Alma Mater Studiorum – Università di Bologna

Scuola di Scienze
Dipartimento di Fisica e Astronomia
Corso di Laurea magistrale in Astrofisica e Cosmologia

# A wide frequency study of the spectral properties of cores and lobes of radio galaxies

Tesi di laurea

Presentata da:
Daniele d'Antonio

Relatore:
Chiar.mo Prof. Gabriele Giovannini

Correlatore:
Dott. Marcello Giroletti

Sessione II
Anno accademico 2016-2017

*to my parents*

*and*

*my sister*

# Sommario

Le osservazioni alle basse frequenze stanno aprendo nuovi scenari per lo studio del cielo, per caratterizzare sia nuovi fenomeni che le già note classi di sorgenti. In questo lavoro vengono caratterizzate le proprietà spettrali della popolazione dei blazar osservati a basse frequenze, vengono comparate le proprietà in banda radio e ad alte energie dei gamma-ray blazars, e vengono cercate le controparti radio delle sorgenti gamma non identificate.

In un precedente lavoro (Giroletti et al. 2016), i 6100 gradi quadrati del Murchison Widefield Array Commissioning Survey catalogue (MWACS) sono stati cross-correlati con il terzo catalogo di nuclei galattici osservati da *Fermi*. Con il lavoro svolto in questa tesi, i 24831 gradi quadrati del Galactic and Extragalactic All-sky MWA (GLEAM) con lo stesso catalogo di *Fermi*. Paragonato ad MWACS, GLEAM non ha solo più grande area di cielo, ma anche una migliore sensibilità e una maggiore copertura spettrale. La frazione di gamma-ray blazars riportati in GLEAM cresce sino a raggiungere il 78%, rispetto al 45% ottenuto con MWACS.

In particulare, sono stati considerati blazar classificati in base alla frequenza del picco di sincrotrone e alle righe di emissione: è stato esaminato il comportamento di oggetti high-, intermediate- e low-synchrotron peaked (HSP, ISP, LSP, rispettivamente) e di flat spectrum radio quasars(FSRQs), BL Lacertae(BLL) e di blazars di tipo non identificato (BCU). L'aumento di detection rate per gli oggetti con picco di sincrotrone a più alta frequenza

(HSP) è notevole: da 9/68 (13%) a 165/270 (61%). Sono quindi state esaminate le proprietà in multi-banda e le proprietà evolutive delle varie classi di oggetti, dal punti di vista della statistica: gli LSP e gli FSRQ sono gli le sorgenti più numerose ad alti redshift, in particolar modo a z 2, mentre gli HSP aumentano a bassi redshift; anche le emissioni in banda X e radio presentano diversi dati statistici: gli HSP presentano una maggiore emissione nell'X rispetto agli LSP e agli FSRQ, ma quest'ultimi presentano maggiore emissione nel radio (sia a basse, a intermedie che ad alta frequenze). Generalmente i BL Lac sono più eterogenei, e presentano molta dispersione nei vari plots. D'altra parte, gli LSP e gli FSRQ coincidono con la stessa sorgente in molti casi. Infatti è stata eseguita una cross-correlazione delle due popolazioni e sono stati osservati molti matches (238 per un totali di 267 FSRQ). Grazie alla grande copertura spettrale a disposizione di GLEAM e di altre survey radio, sono state studiate le proprietà dei blazar a bassa ( 200MHz), intermedia ( 1GHz), e alta frequenza (20GHz con l'Australia Telescope 20GHz, AT20G). Nuclei compatti e lobi estesi hanno differenti proprietà spettrali: a bassa frequenza è stata esaminata l'emissione estesa, mentre ad alta frequenza è stato esaminato il nucleo. Quindi, determinando lo spettro delle sorgenti in diverse bande di frequenza è stato possibile stimare il rapporto tra le due componenti di emissione (componente estesa e componente del nucleo), ed è stata ottenuta una stima della core dominance. La core dominance di un oggetto corrisponde ad un test che verifica l'esattezza del Modello Unificato degli AGN. Gli oggetti con un indice spettrale più piatto sono più core dominated, mentre gli oggetti con indice spettrale più ripido sono più lobe dominated. In generale, il grande campo di vista delle survey a basse frequenze e il grande sviluppo tecnologico in questo campo, in preparazione dello Square Kilometre Array stanno portando una vera e propria rivoluzione.

Infine è stata costruita una simulazione di una survey di oggetti, mediante il linguaggio di programmazione Python, con l'obiettivo di confrotare i dati

misurati con dei dati virtuali e verificare la correttezza del nostro metodo di ricerca. Inoltre per stimare l'emissione del nucleo delle sorgenti a disposizione, è stata utilizzata la survey FIRST Faint Images of the Radio Sky at Twenty, una survey con ottima risoluzione angolare (5 arcsec). L'obiettivo della simulazione è stato quello di verificare quanto questa risoluzione sia effettivamente adatta per studiare l'emissione del nucleo di una radio sorgente.

# Contents

# List of Figures

# List of Tables

# Introduction

This work is a study of the radio spectral properties of the most extreme objects in the class of AGN (Active Galactic Nuclei): the blazars. These sources present relativistic plasma jets closely aligned with the line of sight, and for this reason, these objects are detected at high cosmological distances. Infact the emission is amplified by the Doppler boosting. Their emission is mainly non-thermal with a two-humped spectral energy distribution. The blazars are poorly studied at low frequency, being flat-spectrum sources. However, in this work we show a study of their spectral properties, using the deepest, largest and with best sensitivity survey: the GaLactic and Extragalactic All-sky MWA Survey (GLEAM). Infact it is the first time that it is possible to execute a so accurate study of the blazars at low radio frequency. Moreover, in the last years the astrophysics of the gamma-rays has greatly developed, thanks the advent of the Large Area Telescope (LAT) on board of the *Fermi* satellite. So we studied the possible correlation between radio and gamma-ray emission. This relation is an important issue to understand the emission process for the blazars.
Moreover, we studied the relation between the core emission and the extended emission in AGN. In particular, we examined the behaviour of the core and extended emission with the spectral index, to verify the presence of a flatter spectrum for core dominated objects and of steeper spectrum lobe dominated objects. In other words, we executed a test for the Unified Model of AGN.

Anyway, the thesis is laid out as follows: there are two introductive chapters: the first chapter is a theorical background for AGN (especially blazars), while the second chapter explains the technical features of the strumentation used to create the survey catalogs used in this work. In particular the second chapter shows the characteristics of the Murchison Widefield Array (MWA), a precursor of the Square Kilometre Array (SKA). This is a new generation revolutionary aperture synthesis radio telescope, with a large field of view and a great sensitivity (of the order of the $\mu$Jy), and that will be an ideal instrument to characterize the properties of every kind of radio sources. The third chapter shows the differents cross-correlations between the catalogs used in this work. The cross-correlation allows us to find a counterpart of every source in another frequency range, so it is possible to examine an object in different frequency bands, in different emission regions. The fourth chapter shows the study of the spectral properties for blazars, instead the fifth chapter is the study of the properties of the extended and core emission for AGN.

The work yet explained is the main part of the thesis, but there is a second part in the Appendix, where we show a creation of a simulation of radio sources. The simulation is useful to understand the importance of the core in a radio source, and in general to understand the properties of a survey of radio sources. So we can compare the simulation data with the true data and to obtain some results.

# Chapter 1

# Active Galaxies: theorical background

## 1.1 Active Galactic Nuclei (AGN)

Some galaxies in our universe show a significant excess emission respect that ascribed to stellar processes. These objects are about 1% of the observed galaxies, and they have a typical luminosity about $10^{42}$-$10^{48}$ erg/s. This huge power cannot be only attributed to dust, gas and stars but there is another type of source. It is in the centre of these galaxies, called Active Galactic Nucleus (AGN), while the host galaxy is called active galaxy. The central engine for these galaxies is a supermassive black hole (SMBH) with a mass of $10^6 - 10^9\ M_\odot$, so the surrounding matter must fall towards the centre, causing dissipation of the angular momentum with the formation of an accretion disk. The causes of the dissipation are the viscosity and the turbulent motion of the gas. However, the basic structure is composed by an accretion disk, a Broad Line Region (BLR), a Narrow Line Region (NLR), a thick torus and two jets. We explained that the gas of accretion disk presents dissipation, viscosity and turbulent motion. With these phenomena the adjacent regions of the disk heat each other, so we have thermal emission of a black body. Clearly the disk is affected by the presence of the black hole, in fact it is

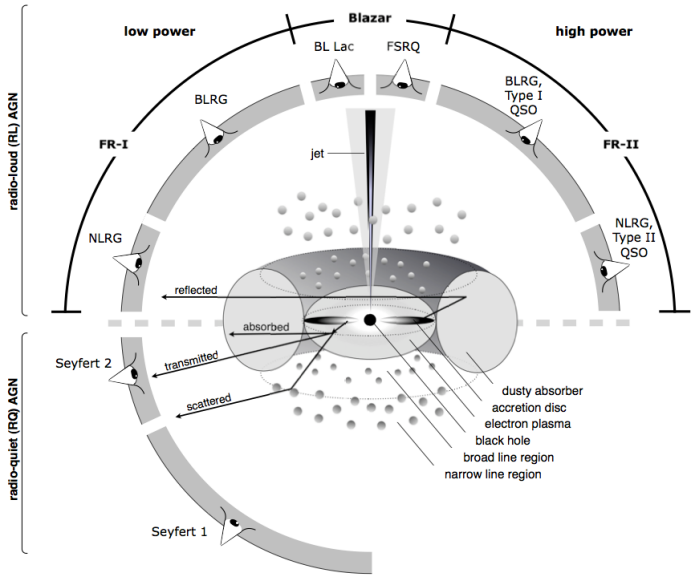


Figure 1.1: a scheme for the AGN Unified Model from Beckmann Shrader et al. 2012. In the top part of the graphic there are the radio-loud sources, in the bottom part there are the radio-quiet sources.

relativity close (about $10^{-3}$ pc). Instead the BLR is about 0.01-0.1 pc from the SMBH, and it is composed by gas with a velocity of about 500-$10^4$ Km/s. So we can observe broad lines in the optical spectrum. At a radius of 1-100 pc, there is the torus that emits in the infrared band by reprocessing the optical/UV photons coming from the disk. At a larger radius (about $10^2$-$10^3$ pc) we can see the NLR. In this region the particles have a lower velocity (up to $10^3$ Km/s) so we observe some narrow lines. In a smaller fraction of objects, the disk is coupled with a pair of relativistic jets. These jets can reach scale of the Mpc order and they are composed by relativistic particles. There are many classes under the name of AGN, with different properties. Also according to the interpretation of the Unified Model for AGN all these sources are the same type object observed from different point of view.

### 1.1.1 AGN classification

On the basis of the ratio between ratio and optical luminosity, AGNs are classified as radio-loud and radio-quiet sources. In particular the Seyfert galaxies, liners and the most populations of the quasars are radio-quiet. Instead, the BL Lacs, some quasars and the radio-galaxies are radio-loud. The radio-galaxies are divided in two categories: Faranoff-Riley Type I (FR I) and Faranoff-Riley Type II (FR II). In FR I radio-galaxies jets are symmetrical, bright and with a big opening angle, so there is an inefficient particles transport. At the end of the jets there are lobes. These objects are bright in the core and they are dark in the external regions. So the FR I radio-galaxies are called *Edge darkened*. Moreover these sources are generally identified with nearby galaxies. Instead, in FR II radio-galaxy jets are collimated (so the transport is efficient), but they are asymmetric and dim. In particular for the FR II the brightest region is in the hot spots in the peripheral areas. So these sources are called *Edge brightened*. Moreover the jets end with some lobes (like in the FR I). Also in the most cases these objects have one jet ($one - side$ sources). The FRII are generally identified with quasars or faraway galaxies. Also the power is different: log P(1.4 GHz)$< 10^{24.5}$ W/Hz for FR I and log P(1.4 GHz)$> 10^{24.5}$ W/Hz for FR II. The reason for these differences is correlated to the accretion rate for the SMBH. In FR II the accretion is more efficient than in the FR I. Also in the last years some studies showed radio-galaxies with a compact morphology, with emission extending at most to 3 Kpc. These sources are called FR 0 and may become a canonical population for the radio-galaxies in the same modality for FR I and FR II (Baldi et al. 2015). However, all radio-galaxies are lobe dominated sources in the radio spectrum. For the Unified Model we observe radio-galaxy with a big angle to the line of sight, while there are some objects with jets closely aligned to the line of sight. They are called blazars, and they are core dominated sources (unlike radio-galaxies). The blazar population is divided in two classes: BL Lacertae (BL Lacs) and Flat Spectrum Radio Quasars (FSRQs). The latter show broad and strong emission lines while BL Lacs do

not have emission lines in the optical spectrum. Moreover both BL Lacs and FSRQ are variable sources. However, this work will show a study mostly about radio and gamma-ray emission for this population. The gamma-ray blazars present a strong emission in both bands. Infact, being jets closely aligned to the line of sight, these objects present Doppler boosting for the emission, so it is amplified. In both bands, the emission has a non-thermal origin: in the radio (and optical/UV) it is synchrotron emission and in the gamma it is inverse Compton.

### 1.1.2 The Spectral Energy Distribution (SED) of blazars

A study with multi-frequency observations can be analyzed with a Spectral Energy Distribution (SED). It composed by a plane $\log(\nu F_\nu)$ vs. $\log(\nu)$ where $\nu$ is the frequency and $F_\nu$ is the flux density. Also we can use $L_\nu$ (luminosity) instead of $F_\nu$. A SED is useful to describe the source power in every frequency range. The SED for a blazar shows two humps which cover the entire frequency interval of the electro-magnetic spectrum. In general at low frequency we have the synchrotron peak (but it can extend from radio until soft X-ray energies) and at high energy we have the inverse Compton peak. As well as a spectroscopic classification, there is a SED classification for the blazars. This blazar classification according to the synchrotron peak position describes three types of objects: Low Synchrotron Peaked (LSP) with $\nu_{\rm peak} < 10^{14}$ Hz, Intermediate Synchrotron Peaked (ISP) with $10^{14}$ Hz $< \nu_{\rm peak} < 10^{15}$ Hz, and High Synchrotron Peaked (HSP) with $\nu_{\rm peak} > 10^{15}$ Hz. Also some previous works (but also this thesis) show that the most of FSRQ are LSP, instead the BL Lacs could be in every populations.
There are two families of models to explain emission of radiation for the blazars: the hadronic models and the leptonic models. For the hadronic models the observed emission is generated by relativistic protons within the jets. The protons interact with the surrounding photons, producing $e^{\pm}$ pairs. The latter are accelerated by a magnetic field, producing synchrotron radiation and the first hump in the SED. The second hump is originated by

the interaction between $e^{\pm}$ pairs and photons. In other words, the $e^{\pm}$ pairs provide energy to the sorrounding photons with the inverse Compton process. Also the secondo hump is generated even with the decay of particles originated from the interaction proton-proton. For the leptonic models the radiation is generated from electrons in the jets. These particles are accelerated in a magnetic field, producing synchrotron radiation and they provide energy to photons generating inverse Compton hump. So the two families models are similar but the origin is different: in the hadronic models the origin of the radiation is in the protons while in the leptonic models is in the electrons. However, the protons are more massive than electrons, so the acceleration efficiency is lower for the protons. Also they have longer cooling time. So to produce the observed emission we need a stronger magnetic field (of the order of tens of Gauss) and with this modality we have emission at high frequency. Moreover, some results favor the leptonic models:

1)for high energies and low frequency we have a similar trend of the two humps, so we can think that the emission in the two energy range are generated by the same particles;
2)in some sources, if a peak is higher or lower, we can see the same behaviour in the other peak;
3)if we have variability at low frequency we usually have variability at high energies.

Another interesting property of the SED for a blazar is the relation between luminosity and the peak frequency. When both peaks move to lower frequency the power increases. Infact, in general the LSPs are more luminous than HSPs. Also in the most luminous sources (and in the most powerful) we have a larger photon density, so the electrons have a better cooling efficiency. In other words, the electrons cool in a shorter time because the density photons is larger (Ghisellini et al. 1998). So the emission is at lower frequency, and the peak frequency at low frequency is related to the intensity of the

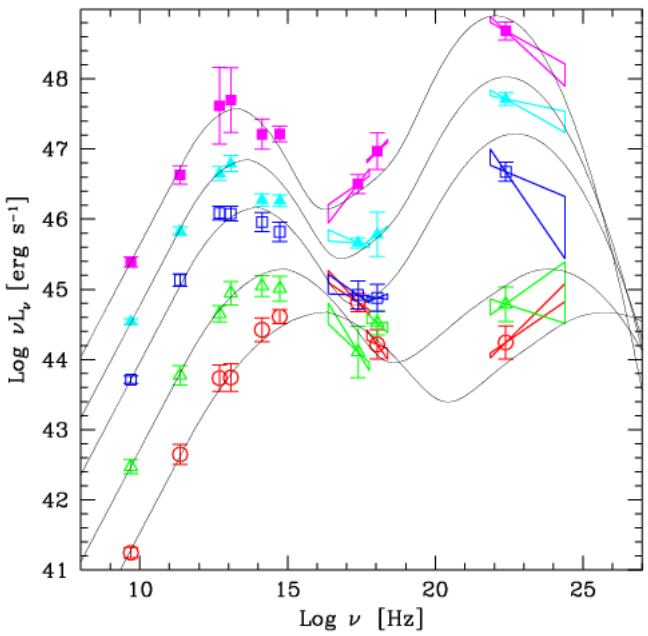


Figure 1.2: Spectral Energy Distribution for a blazar, with the synchrotron peak (left) and the inverse Compton peak (right). In the most luminous sources the synchrotron peak and the IC peak are at lower frequency (Donato et al. 2001).

magnetic field and the energy distribution function for the electrons.

# Chapter 2

# Observing instruments

## 2.1 A precursor for SKA: the Murchison Widefield Array (MWA)

The Square Kilometre Array (SKA) is a new generation radio telescope. It will use data from many antennas distributed over more than 3000 kilometers, to synthesise a new radio telescope with a big collecting area and a very large field of view. However, in this work we used the data from MWA, a precursor of SKA. MWA is a low-frequency radio telescope (it operates between 80 and 300 MHz) and it is located in the desert, in Western Australia. Moreover it is composed by 2048 dual-polarization dipole antennas arranged as 128 tiles (each a 4x4 array of dipoles) with 8128 baselines. The collecting area is about 2000 square meters while the field of view is approximately between 15 and 50 degrees.

The values for the angular resolution are showed in the table 2.1.

The MWA has been used to carry out two surveys of the sky at low frequency. The corresponding catalogues are: the Murchison Widefield Array Commisioning Survey (MWACS) and the GaLactic and Extragalactic All-sky MWA (GLEAM).

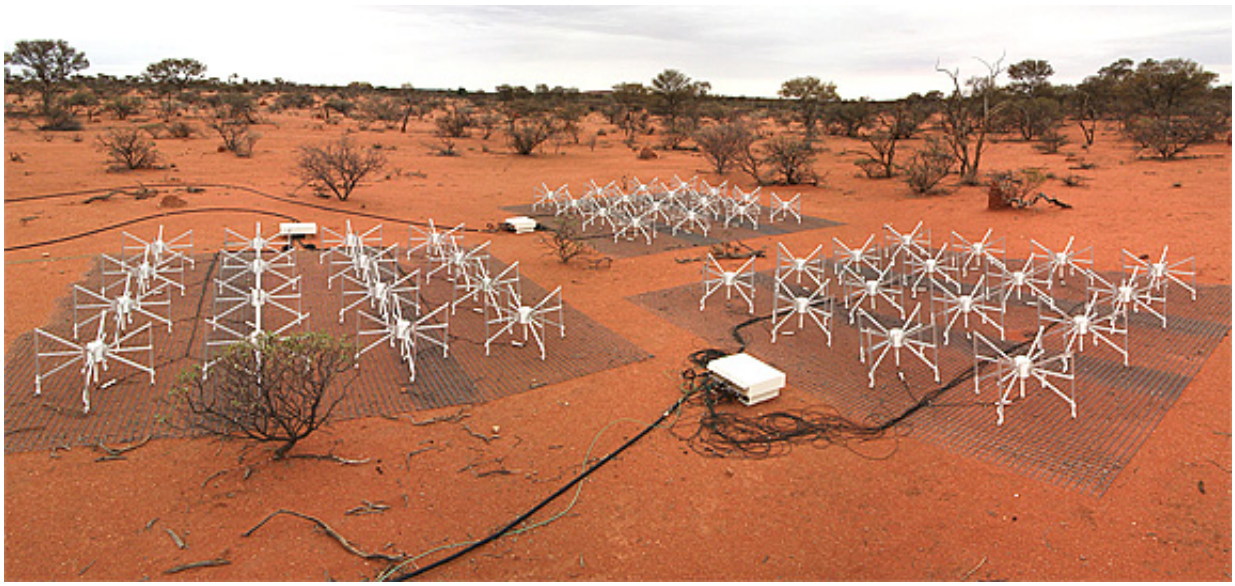

Figure 2.1: MWA is located in the australian desert, in the Western Australia

| baseline | frequency | angular resolution |
|---|---|---|
| 1.5 Km | 150 MHz | $\sim$ 3 arcmin |
| 3 Km | 150 MHz | $\sim$ 2 arcmin |
| 1.5 Km | 200 MHz | $\sim$ 2 arcmin |
| 3 Km | 200 MHz | $\sim$ 1 arcmin |

Table 2.1: angular resolution for the MWA.

### 2.1.1 The Murchison Widefield Array Commisioning Survey (MWACS)

This survey covers the sky in the region between 0°$\leq$ RA $\leq$ 127.5° or 307.5° $\leq$ RA $\leq$ 360° and -58.0° $<$ Dec $<$ -14.0°. The observations were done in October 2012. All the sources of the catalogue have high absolute Galactic latitude and the 3LAC (the catalogue of the *Fermi* satellite for the blazars) presents object in the same area. So the high Galactic latitude is ideal to study the properties of blazars. The primary work about MWACS is published in Hurley-Walker et al. 2014. The technical features are reported

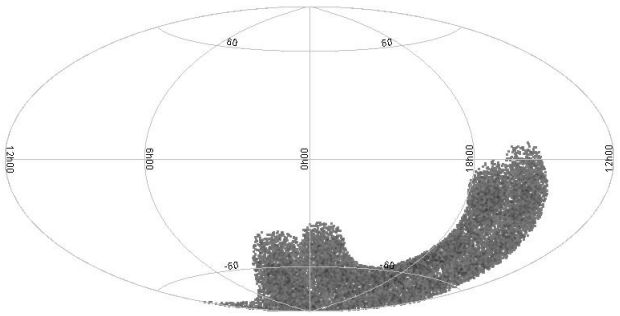


Figure 2.2: Survey of the MWACS with galactic coordinates (Hurley-Walker, et al. 2014). The dark regions are the areas with largest source density.

in the table:

| | |
|---|---|
| observation band | centered at 119, 150, 180 MHz |
| covered area | 6100 sq. deg. |
| number sources | 14110 |
| source density | $2.31/\text{deg}^2$ |
| sensitivity | 50 mJy/beam (from 120-180 MHz) |
| angular resolution | $\sim$ 180 arcsec |

Table 2.2: technical features for the MWACS

### 2.1.2 The GaLactic and Extragalactic All-sky MWA (GLEAM)

After the completion of MWACS, the MWA was used to carry out a larger and deeper sky survey: the Galactic and Extragalactic All-sky MWA (GLEAM) survey. GLEAM observing began in August 2013 and the first year concluded in July 2014. The second year of observing concluded in July 2015. A third year of observing at high ( 250-310 MHz) frequency concluded in July 2016. The primary work about GLEAM is published in Hurley-Walker et al. 2017.

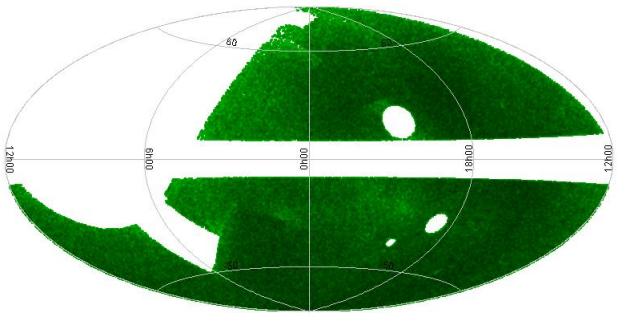


Figure 2.3: Survey of the GLEAM with galactic coordinates (Hurley-Walker, et al. 2017). The dark regions are the areas with largest source density.

We can see from MWACS to GLEAM both the total number of sources and the surface density grow. In fact with GLEAM we have a larger covered area, a better sensitivity resulting in a larger number of source. In particular the GLEAM survey covered the entire southern sky, except the Magellanic Clouds and Galactic latitude within 10 deg from the Galactic plane.

These catalogues are mainly composed by extra-galactic sources and we expect that GLEAM will improve our knowledge about the low-frequency spectrum of the Active Galactic Nuclei at low and high redshift. Moreover with these data it is possible to research new information about relics and halos in galaxy clusters. Also the investigation for new notions for the cosmology is a possible field of research. However, in this work we examined the characteristics of blazars. The technical features are reported in the table:

| | |
|---|---|
| observation band | 72-231 MHz |
| covered area | 24831 sq. deg. |
| number sources | 307455 |
| source density | $12.3/\mathrm{deg}^2$ |
| sensitivity | 6-10 mJy/beam |
| angular resolution | $\sim$ 100 arcsec |

Table 2.3: technical features for the GLEAM

Figure 2.4: The Very Large Array is located in New Mexico, USA.

## 2.2 The Very Large Array (VLA)

The Very Large Array (VLA) is an interferometer composed by 27 radio antennas in the Plains of San Agustin (80 Km west of Socorro, New Mexico, USA). Every antenna has a diameter of 25 meters. The data of the antennas is combined to obtain the sensitivity of an antenna with a diameter of 130 meters and an angular resolution varying between approximately 0.1" and 45". We used two catalogues of the VLA: the NRAO VLA SKY SURVEY (NVSS)(Condon et al. 1998) and the Faint Images of the Radio Sky at Twenty (FIRST)(Becker et al. 1995).

### 2.2.1 The NRAO VLA SKY SURVEY (NVSS)

The NRAO VLA Sky Survey was obtained with the VLA between 1993 September and 1996 October. Other observations were made in the last four months of 1997. The catalogue contains galactic and extra-galactic sources. There are quasars and radio galaxies, most of the galaxies in the IRAS Faint Source Catalog (Moshir et al. 1992), ultra-luminous starburst galaxies even at cosmological distances, low luminosity AGNs, Galactic planetary nebulae, pulsars and stars. The survey covered 82 % of the entire sky. The technical features are reported in the table:

| | |
|---|---|
| observation band | centered at 1.4 GHz |
| covered area | 33827 sq. deg. |
| number sources | $\sim 1 \times 10^6$ |
| source density | $\sim 53/\mathrm{deg}^2$ |
| sensitivity | 1.11 mJy/beam |
| angular resolution | 45 arcsec |

Table 2.4: technical features for the NVSS

### 2.2.2 The Faint Images of the Radio Sky at Twenty (FIRST)

The First Survey is a project realized using the VLA in the more extended configuration. With this configuration we have a 10 times better angular resolution respect to the configurations of the NVSS. The survey area has been chosen to coincide with that of the Sloan Digital Sky Survey (SDSS) (about 80% of the north sky and 20% south sky). In particular with a limit $m_{\mathrm{v}} \sim 23$ for the SDSS, about 40% of the counterparts to FIRST objects are detected.

| | |
|---|---|
| observation band | centered at 1335, 1730 MHz |
| covered area | 10000 sq. deg. |
| number sources | $\sim 900000$ |
| source density | $\sim 90/\mathrm{deg}^2$ |
| sensitivity | 1 mJy |
| angular resolution | 5 arcsec |

Table 2.5: technical features for the FIRST

Figure 2.5: The Australia Telescope Compact Array (ATCA) is located at $\sim$ 500 km north-west of Sydney, (Australia).

## 2.3 The Australia Telescope Compact Array (ATCA)

The Australia Telescope Compact Array is composed by six antennas with a diameter of 22 m and the baselines are 1.5, 3 and 6 Km. It is possible to use the array both at low-frequency (less than 1GHz) and at high frequency (20 GHz). We used a catalogue of the ATCA: the Australia Telescope 20-GHz Survey (AT20G) to study the emission for the AGN at high frequency.

### 2.3.1 The Australia Telescope 20-GHz Survey (AT20G)

The Australia Telescope 20-GHz Survey (AT20G) is a radio survey at 20 GHz, composed in the period from 2004 to 2008. It covers the whole sky south of declination 0 degrees. It is the largest and most sensitive survey of the sky at this frequency, which is crucial for the study of radio emission from flat-spectrum sources, such as the cores of radio-loud AGNs. The catalogue presents 5890 objects above 20 GHz as well as follow up measurements at 5 and 8 GHz. The technical features are reported in the table:

| | |
|---|---|
| observation band | centered at 5,8,20 GHz |
| covered area | 20086 sq. deg. |
| number sources | 5890 |
| source density | $\sim 0.29/\mathrm{deg}^2$ |
| sensitivity | 40 mJy |
| angular resolution | 0.15 arcsec |

Table 2.6: technical features for the AT20G

## 2.4 The Roma BZCat

The BZCat is a multi-frequency catalog for blazars, and it is regularly updated since the release of the first edition (Massaro et al. 2009). The latest (fifth) edition (Massaro et al. 2015) reports data for 3561 objects. In particular coordinates, redshift and data of different bands (radio, millimetre, optical, X-rays and gamma-rays). All sources are detected at radio wavelength, and the radio data come from other catalogues: NVSS and FIRST at 1.4 GHz and SUMSS at 0.8 GHz. The technical features are reported in the table:

| | |
|---|---|
| observation band | radio (0.8,1.4 GHz), millimetre, optical, X, gamma |
| covered area | 41253 sq. deg. (entire sky) |
| number sources | 3561 |
| source density | $\sim 0.09/\mathrm{deg}^2$ |
| sensitivity | $\sim$ 1.6 mJy/beam (radio data) |
| angular resolution | 5, 45 arcsec, $\sim$ 1 arcmin (radio data) |

Table 2.7: technical features for the BZCat

## 2.5 The Sloan Digital Sky Survey (SDSS)

The SDSS catalog contains five-band photometry for 357 million objects. There are over 1.6 million spectra in total 930,000 galaxies, 120,000 quasars and 460,000 stars. This survey is realized to obtain CCD images over 10,000 $\deg^2$ of high-latitude sky, and spectroscopy of a million galaxies and 100,000 quasars over the same region. The primary work of this survey is York et al. 2000 and the latest (seventh) edition is released from Abazajian et al. 2009.

| | |
|---|---|
| observation band | 3800-9200 Å |
| covered area | 11663 sq. deg. |
| number sources | $\sim$ 357 million |
| source density | $\sim$ 30600 /$\deg^2$ |
| S/N (signal/noise) | 10 per pixel |
| resolution $\lambda/\Delta\lambda$ | $\sim$ 2000 |

Table 2.8: technical features for the SDSS

## 2.6 The *Fermi* satellite

The Gamma-ray Large Area Space Telescope (GLAST), later called *Fermi* Gamma-ray Space Telescope, is the successor of the Energetic Gamma Ray Experiment Telescope (EGRET), that operated from 1991 to 2000. The satellite was launched on June 11, 2008 on an elliptical orbit at altitude of about 565 Km, with an inclination of 25.6° respect to the Earth's equator (Atwood et al. 2009). *Fermi* treads the full orbit in about 96 min, also in about 3 hours it scan the entire sky. On board the satellite there are two instruments: the Large Area Telescope (LAT) and the Gamma-ray Burst Monitor (GBM). The LAT is a pair conversion telescope and detects gamma rays between $\sim$ 20 MeV and $\sim$ 300 GeV, with a field of view of 2.4 sr, and an

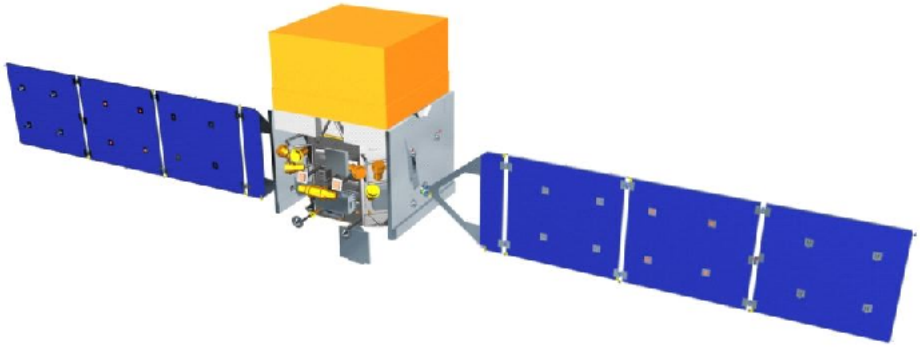

Figure 2.6: rappresentation of the *Fermi* satellite.

angular resolution $< 0.15°$ for $E > 10$ GeV. *Fermi* works at high energy of the electromagnetic spectrum, so the strumentation detects individual photons. So about the resolution we must talk about the single photon angular resolution. Infact at high energy every source emits few photons. The LAT presents a tracker, in which gamma rays decay into electron-positron pairs, and a calorimeter, which measures the energy of the pairs. Moreover the external surface of the tracker is covered by an anti-coincidence detector. The latter allows to reject cosmic rays. Instead, the GBM is useful to study of transient phenomena between 8 keV and 40 MeV, and it is a complementary instrument while the LAT is the primary instrument on the *Fermi* satellite. The *Fermi* project is a work of NASA with the collaboration of Italy, Germany, France and Japan.
The mission is an opportunity to examine high energy phenomena from gamma-ray burst, AGN, pulsars, supernova remnants, binary systems and flares from the sun.

### 2.6.1 The third catalogue of the Fermi-LAT (3FGL)

The third catalogue of the *Fermi* satellite (3FGL) (Acero et al. 2015) is a catalogue of gamma-ray sources observed by *Fermi* in the first 4 years of the mission, and it is the successor to the LAT Bright Source List (0FGL), the First *Fermi* LAT (1FGL) and the Second *Fermi* LAT (2FGL) catalogues.

The new 3FGL catalog is deeper than the previous catalogues in the 100 MeV-300 GeV energy range. The sources are not distributed evenly. Infact 468 objects are located on the Galactic plane. We reported the features for 3FGL in the table:

| | |
|---|---|
| observation band | 100MeV-300GeV |
| covered area | 41253 sq. deg. (entire sky) |
| number sources | 3033 |
| source density | $0.07/\text{deg}^2$ |

Table 2.9: technical features for the 3FGL. We can see that the source density is very low compared to the source density in the radio surveys

| energy value | per-photon angular resolution |
|---|---|
| 100 MeV | $\sim 5^\circ$ |
| 1 GeV | $0.8^\circ$ |
| above 20 GeV | $\sim 0.2^\circ$ |

Table 2.10: angular resolution for the 3FGL. The resolution rises to the drop in energy. Infact the resolution varying with energy approximately as $E^{-0.8}$.

### The third LAT AGN Catalogue (3LAC)

Most of the 3FGL sources are blazars, and these objects compose a subset of the 3FGL: the 3LAC. Infact the 3LAC sources are identified with AGNs. The catalogue contains accurate positions for the low frequency counterparts and information about the multiwavelength properties: redshift, radio, optical and X-ray flux, position of the peak of the synchrotron component of the Spectral Energy Distribution (SED). In particular the subset is composed by 680 Low Synchrotron Peaked (LSP), 296 Intermediate Synchrotron Peaked (ISP), 393 Low Synchrotron Peaked (LSP), sources in according to the SED

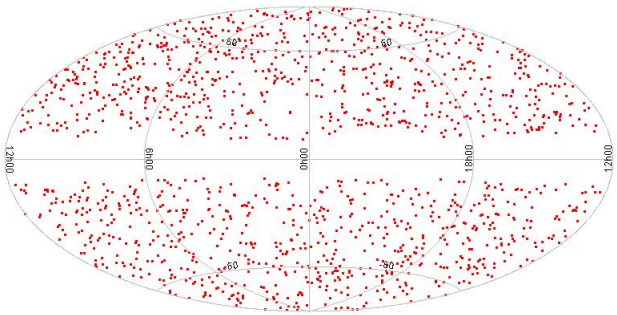


Figure 2.7: Survey of the 3LAC with galactic coordinates (Ackermann, et al. 2015).

classification; and it presents 414 Flat-Spectrum Radio Quasar (FSRQ), 604 BL Lacertae (BL Lacs) and 402 Blazar Candidate Unidentified (BCU), and the latter are blazars but we are not sure about which kind of blazar.

### Redshift distribution

Let us consider the redshift distribution of these objects. The LSP and FSRQ are at larger redshift then other sources. This suggests that many LSP are FSRQ. Also we must consider many BL Lacs have not a value for the redshift so it is not possible to report all objects in a redshift distribution. However, in the 3LAC we have objects with a redshift in the range between 3.104 and 0.0018 so we see sources both high and low redshift.
In the figure 2.8 we see the redshift distributions for FSRQs, BL Lacs and BCUs. There are sources of the 3LAC and of the 2LAC. The latter is the Second Catalog of Active Galactic Nuclei detected by *Fermi* and it is the previous catalog of the 3LAC. For the FSRQs the distribution of the 3LAC sources and the distribution of the 2LAC sources are similar. The two distributions show that the number density of FSRQs grows drammatically up to redshift $z \sim$ 0.5-2.0. For $z < 2$ the two distributions decline (Ajello et al. 2012).
Also for the BL Lacs the distribution of the 3LAC sources and the distribution of 2LAC sources are similar, with a maximum near z=0.3. In the

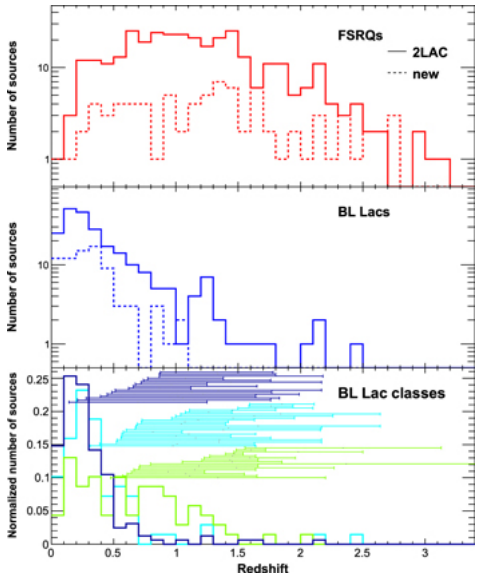


Figure 2.8: redshift distributions (solid: 2LAC sources; dashed: new 3LAC sources) for FSRQs (top), BL Lacs (middle), and different types of BL Lacs (bottom): LSPs (green), ISPs (light blue), and HSPs (dark blue). The ranges between the lower and upper limits are also depicted in the bottom panel when both limits are available (Ackermann et al. 2015).

figure there are different kinds of BL Lac: LSP, ISP and HSP. The redshift distributions gradually spread out to higher redshifts from HSP-BL Lacs to LSP-BL Lacs.

### Flux and photon spectral index

The Fig. 2.9 shows the photon index distributions for different blazars classes (FSRQs, BL Lacs, BCUs). The distributions report the sources of the 2LAC and the 3LAC. The sources detected in the 3LAC are slightly softer than the 2LAC sources. In other words, with the new catalog it is possible to detect lower energy peaked blazars. Instead, there is no differences for the two samples of BL Lacs. For the BCUs the distribution of the 3LAC extends at larger values for the photon spectral index. Also we see the FSRQs present a larger photon spectral index than the BL Lacs.

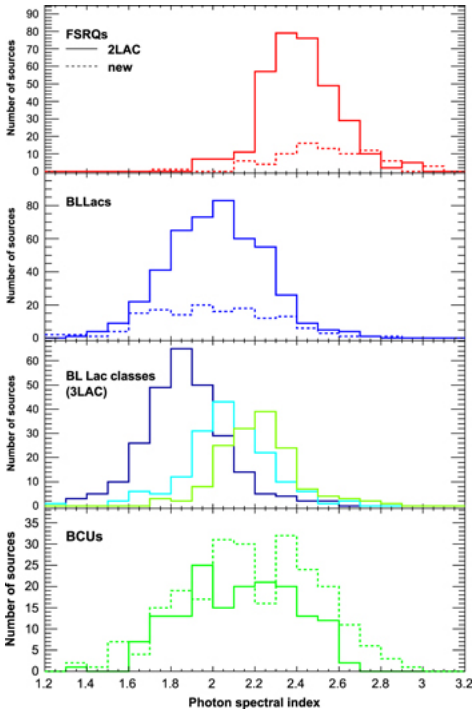


Figure 2.9: Photon spectral index distributions. Top: FSRQs (solid: 2LAC sources; dashed: new 3LAC sources). Second from top: BL Lacs (solid: 2LAC sources; dashed: new 3LAC sources). Third from top: 3LAC LSP-BL Lacs (green), ISP-BL Lacs (light blue), and HSP-BL Lacs (dark blue). Bottom: blazars of unknown type (solid: 2LAC sources; dashed: new 3LAC sources) (Ackermann et al. 2015).

The Fig. 2.10 shows the photon index versus the photon flux with the detection limit. In particular the detection limit of the 3FGL (solid line) is better than the detection limit of the 2FGL (the Second Catalog of *Fermi* and previous catalog of the 3FGL). Also in this figure we can see that the FSRQs are the objects with the largest photon index.

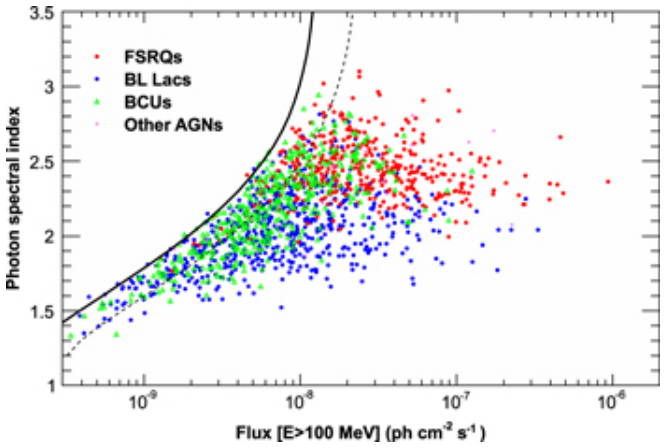


Figure 2.10: Photon spectral index vs. photon flux above 100 MeV for blazars in the 3LAC Sample. Red circles: FSRQs; blue circles: BL Lacs; green triangles: blazars of unknown type; magenta stars: other AGNs. The solid (dashed) curve represents the approximate 3FGL (2FGL) detection limit based on a typical exposure. The 2FGL is the second catalog of *Fermi* while the 3FGL is the third catalog (Ackermann et al. 2015).

# Chapter 3

# Cross-correlations of catalogues

In this chapter we report all cross-correlations of the catalogues executed in this work.

The new low-frequency radio data are opening a new window for the study of the sky, especially for the blazars. These objects are so poorly studied at low frequency and now we can better characterize known source classes.

In a previous work (Giroletti et al. 2016), the authors cross-correlated the 6100 deg$^2$ of the MWACS with the sources of the BZCat and the 3LAC. They found low frequency counterparts for 186 out of 517 (36%) blazars, 79 out of 174 (45%) gamma-ray blazars. The limited detection rate caused a selection bias. Infact the lower sources (especially BL Lacs) were under-represented. Similar biases affected earlier works by Massaro et al. 2013 and Nori et al. 2014. In this thesis we cross-correlated the 24831 deg$^2$ of the GLEAM with the 3LAC. So we have a larger number of data to analyse. Infact we showed in the chapter 2 the properties for GLEAM and MWACS, and we know with GLEAM, we have a deeper survey, with more sources, a better sensitivity and less affected by selection bias. In other words, this is the first time that the spectral properties of blazars at low frequency can be discussed with a large and representative data sets.

Also we done also cross-correlations for other catalogues that we report in this chapter.

## 3.1 Cross-correlation for the GLEAM and the 3LAC

We cross-matched the two catalogues, using a positional uncertainty of 1" for the 3LAC sources and the uncertainty reported in the catalogue for GLEAM. The value of 1" for the error of the 3LAC is a reasonable estimate, considering the values for the errors of the catalogues which contain the counterparts at radio frequency of the gamma-ray sources. Infact in the 3LAC, the radio counterparts come from different surveys: AT20G, NVSS, SUMSS, FIRST and PMN surveys. Every survey presents a particular angular resolution and a particular frequency. So in every survey there is a value for the error, and the latter is different comparated another error of another survey. Moreover, the most blazars selected are calibrators for the VLBI (Very Large Baseline Interferometry), and their position is known with an uncertainty of the order of the milliarcosecond, so 1" is very conservative choice. Anyway more information are reported in Ackermann et al. 2015.
Therefore from the 307455 sources in the GLEAM and from the 1444 sources in the 3LAC (963 in the GLEAM sky), we obtained 747 matches (blazars): 424 LSP, 131 ISP, 165 HSP for the SED classification, and 267 FSRQ, 257 BL LACS, 214 BCU for the spectroscopic classification. Also 747 objects is an high detection rate, infact we estimated 963 gamma-ray sources in the sky of the GLEAM. In other words, the most blazars are detected at low frequency.
Moreover, we created a false 3LAC with inverted declination, to verify the correct efficiency of the cross-correlation between the GLEAM and the 3LAC. So we cross-correlated the false 3LAC with the GLEAM and we obtained 75 matches. This number is much smaller than 747 (number of the matches for the true 3LAC), infact this means that the fraction of spurious matches in our cross-correlation is about 10%. Therefore we concluded that we executed a good cross-correlation because the matches are right. Moreover the 3LAC have not the gamma fluxes, unlike the 3FGL. So we cross-correlated

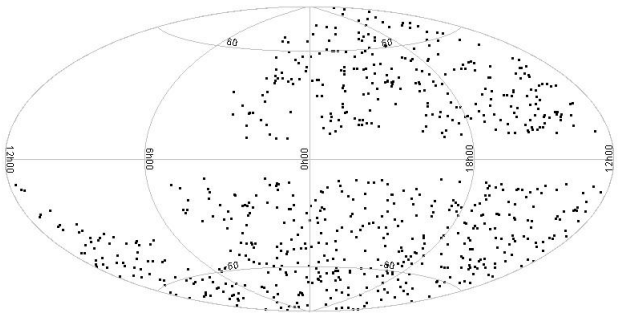


Figure 3.1: Survey of the blazars with a counterpart at low-frequency (3LAC vs. GLEAM). Obviously the sources are in the sky area of the GLEAM survey.

the two catalogues to obtain the gamma flux for the 3LAC sources. We cross-correlated the two samples, identifying the matches with the sources with the same name.

## 3.2 Cross-correlation for the AT20G and the 3LAC

We cross-correlated the 3LAC with the AT20G. The former present 1444 sources and the latter contains 5890 sources and with the cross-correlation we obtained 392 matches. So these sources are selected blazars at high frequency. This selection is useful to study the emission from the core of the radio sources. However, analyzing the position of the synchrotron peak, these sources are 292 LSP, 57 ISP, 36 HSP. Instead for the spectroscopic classification they are 179 FSRQs, 96 BL Lacs, 113 BCUs.

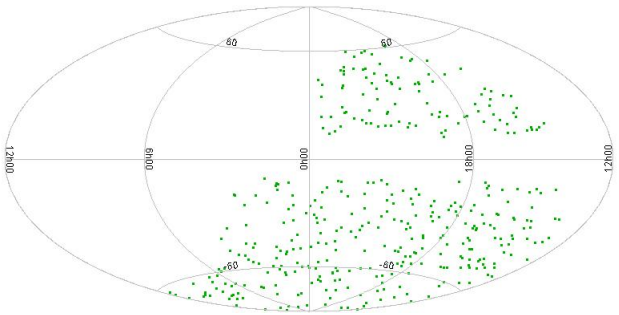


Figure 3.2: Survey of the detected blazars at high frequency (3LAC vs. AT20G). The most objects are in the Southern sky. Infact the most sources of the AT20G are in the same sky.

## 3.3 Cross-correlation for the AT20G and the GLEAM

We remember that the AT20G has 5890 objects and the GLEAM has 307455 objects.
This cross-matches are done using the same algorithm of the previous sections. In other words, we obtained some radio sources at low and high frequency. The number of the matches is 4271. The cross-correlation represents a method to compare the core emission (at high frequency) and the extended emission (at low frequency). In particular if we estimate the ratio between $S_{\mathrm{AT20G}}$ and $S_{\mathrm{GLEAM}}$, we expect that a core dominated source (like a blazar) will have a larger ratio than a lobe dominated source (like a radio-galaxy). In the next chapters we will show this behaviour. Moreover, the AT20G catalogue have not a spectroscopic classification, so we obtained the optical counterparts from Mahony et al. 2011. Therefore we cross-matched the optical catalogue (composed by 5890 objects) with the AT20G, identifying the matches with the objects with the same name.

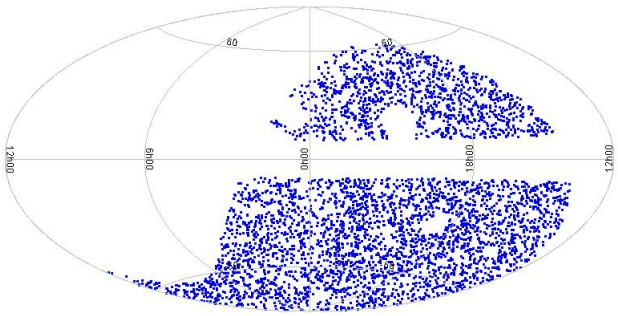


Figure 3.3: Survey for radio sources at low and high frequency (AT20G vs. GLEAM).

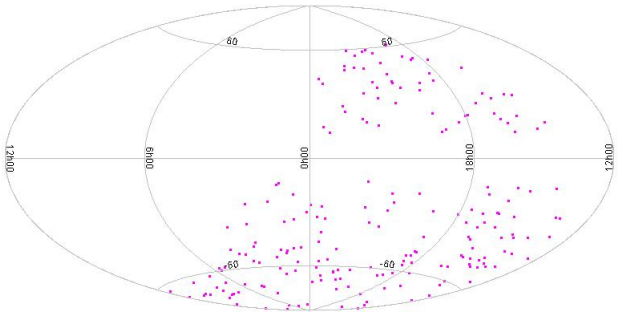


Figure 3.4: Survey for blazars selected at low and high frequency (3LAC vs. AT20G-GLEAM).

## 3.4 Cross-correlation for the 3LAC and AT20G-GLEAM

We cross-correlated the 3LAC with the generated catalogue from the cross-correlation between AT20G (5890 sources) and GLEAM (307455 sources). Therefore, we created a survey with 208 gamma-ray blazars at low and high frequency: 171 LSPs, 16 ISPs, 21 HSPs and 151 FSRQs, 36 BL Lacs, 19 BCUs.

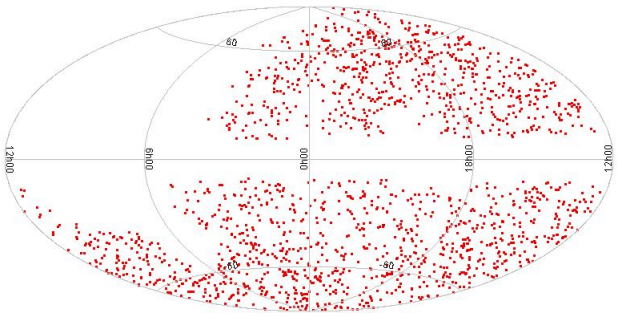


Figure 3.5: Survey radio sources at low and intermediate frequency (BZCat vs. GLEAM).

## 3.5 Cross-correlation for the BZCat and GLEAM

We cross-correlated the 3561 sources of the BZCat with the 307455 sources of GLEAM, using the usual method, and we extracted 1709 matches: 1122 FSRQs, 442 BL LACs and 141 BCUs. We have not a classification for the position of the synchrotron peak in the sample. In general, in a sample the LSPs and the FSRQs are the most objects of the entire population, and in this catalogue we can see that the FSRQs rappresent a very large number compared to the other classes. This suggests that the FSRQs are brightest.

## 3.6 Cross-correlation 3LAC-GLEAM and BZCat-GLEAM

In the previous sections we described the cross-correlations 3LAC-GLEAM and BZCat-GLEAM. Then we cross-correlated the two catalogues obtained. For the sample 3LAC-GLEAM we have 747 sources and for the sample BZCat-GLEAM we have 1709 sources. Therefore, executing this cross-match, we selected blazars at low and intermediate frequency. The new sample cointains 530 sources: 331 LSPs, 88 ISPs, 106 HSPs and 239 FSRQs, 248 BL Lacs, 40 BCUs. We see that the number of BL Lacs is larger than the number of FSRQs. In general the opposite is true. Anyway we must consider that

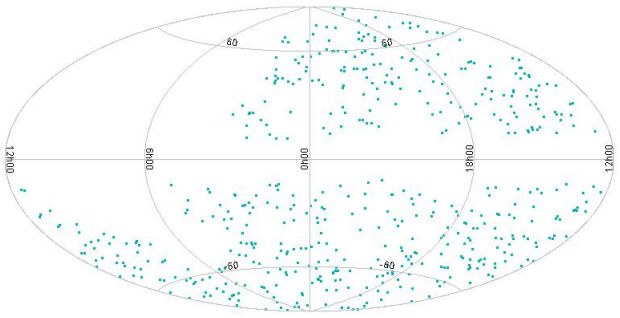


Figure 3.6: Survey for the blazars selected at low and intermediate frequency (3LAC-GLEAM vs. BZCat-GLEAM).

we have 40 candidate blazars, and we do not know which kind of blazars they are. It needs to be noted that in the 3LAC there are many sources that are classified as blazar candidates on the basis of their multi-wavelength properties, yet they lack spectroscopic information. As such, they are not confirmed blazars and they do not appear in the BZCat master list. Indeed they form the bulk of the 747-530=217 sources missed in this cross-correlation.

## 3.7 Anticross-correlation BZCat-GLEAM and 3LAC-GLEAM

We executed an anticross-match between BZCat-GLEAM (1709 objects) and 3LAC-GLEAM (747 objects). So we obtained a sample composed by 1179 objects with 883 FSRQs, 193 BL Lacs, 101 BCUs. These are blazars that are detected by GLEAM but not by *Fermi*. We have not the SED classification for these sources.

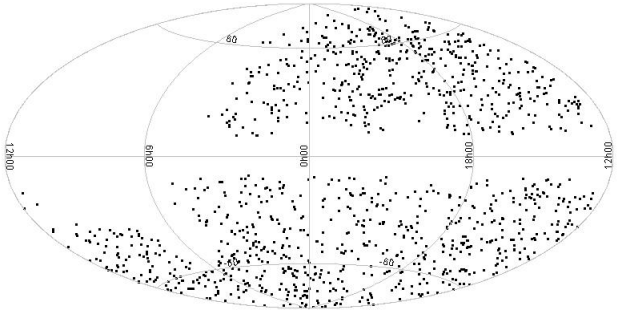


Figure 3.7: Survey for the anticross-correlation BZCat-GLEAM and 3LAC-GLEAM.

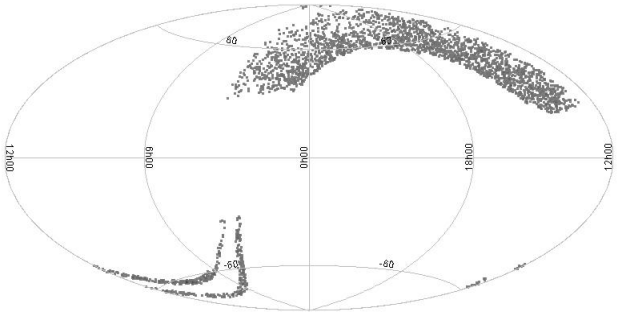


Figure 3.8: Survey of radio sources selected at low and intermediate frequency (SDSS, FIRST, NVSS, GLEAM).

## 3.8 Cross-correlation for SDSS-FIRST-NVSS and GLEAM

The SDSS-FIRST-NVSS (18286 objects) (Best et al. 2011) is a sample with the combined data from SDSS, FISRT and NVSS. We cross-correlated this catalogue with the GLEAM (307455 objects). With this cross-correlation we achieved 2906 sources. We divided the sample in three populations: objects with the flux density of the FIRST $S_{\mathrm{FIRST}} = 0$, with the density flux of the FIRST $S_{\mathrm{FIRST}} \neq 0$, and the sources of the radio-class 1. We will explain the details and the motivations for this division in the chapter 5.

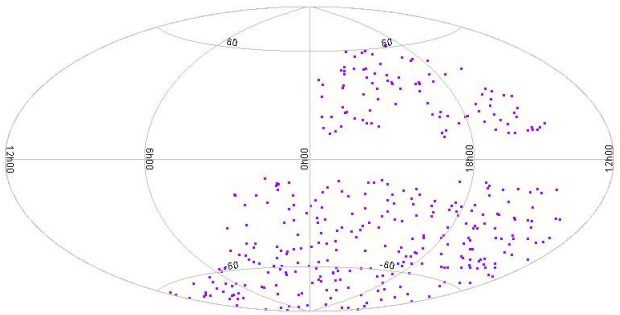


Figure 3.9: Survey of blazars detected at low and high frequency (3LAC-GLEAM vs. 3LAC-AT20G).

## 3.9 Cross-correlation 3LAC-GLEAM and 3LAC-AT20G

We cross-correlated the sample of the blazars detected at low frequency (3LAC-GLEAM), composed by 747 objects, with the sample of the blazars detected at high frequency (3LAC-AT20G), composed by 392 objects. Therefore we generated a sample with 367 objects. We will use this new sample to study the nuclear properties of blazars in Chapter 5.

## 3.10 Statistics

In this section we report a summary to describe the statistical data about the samples generated. We do not report the statistical data for the cross-correlation between the GLEAM with the 3LAC: we will report these data in the next chapter.
With the cross-correlation 3LAC vs. AT20G we see the blazars detected at high frequency, and we can see that the most blazars are detected at low frequency.
The detection rate for the cross-match AT20G vs. GLEAM is high (88%), so in the most cases if a blazar emits at low frequency it also emits at high frequency.

While for the cross-correlation 3LAC vs. GLEAM-AT20G the detection rate is not so high (only 31%), so the blazars detected both at high and low frequency are not many objects.
The BZCat is the most complete catalog for blazars in the literature, and the most blazars of this catalog are detected at low frequency, infact the detection rate for the cross-match BZCat vs. GLEAM is 76%.
In the cross-correlation 3LAC-GLEAM vs. BZCAT-GLEAM we estimated the number of blazars of the BZCat detected at low frequency are detected at high energies (gamma-rays). The detection rate (71%) suggest a correlation between gamma emission and radio emission. However we will explain this relation in the chapter 4.
The cross-correlation FIRST-SDSS-NVSS vs. GLEAM is a comparison between low and intermediate frequency and the detecton rate is not high (only 26%). Anyway we must consider that the presence of differents angular resolutions for many catalogues.
The cross-match 3LAC-GLEAM vs. 3LAC-AT20G presents blazars at high and low frequency, and the detection rate is close to half of the entire sample selected (49%).

| class | number matches | number sources | detection rate |
|---|---|---|---|
| total | 392 | 655 | 60% |
| FSRQ | 179 | 191 | 94% |
| BCU | 113 | 256 | 44% |
| BLL | 96 | 202 | 48% |
| LSP | 292 | 324 | 90% |
| ISP | 57 | 107 | 53% |
| HSP | 36 | 180 | 20% |

Table 3.1: statistical data for the cross-match 3LAC vs. AT20G.

| class | number matches | number sources | detection rate |
|---|---|---|---|
| total | 4271 | 4858 | 88% |

Table 3.2: statistical data for the cross-match AT20G vs. GLEAM. We have not data for SED and spectroscopic classifications.

| class | number matches | number sources | detection rate |
|---|---|---|---|
| total | 208 | 665 | 31% |
| FSRQ | 151 | 192 | 79% |
| BCU | 19 | 259 | 7% |
| BLL | 36 | 207 | 17% |
| LSP | 171 | 330 | 52% |
| ISP | 16 | 109 | 15% |
| HSP | 21 | 182 | 12% |

Table 3.3: Statistical data for the cross-match 3LAC vs. AT20G-GLEAM

| class | number matches | number sources | detection rate |
|---|---|---|---|
| total | 1709 | 2238 | 76% |
| FSRQ | 1122 | 1272 | 88% |
| BCU | 141 | 189 | 75% |
| BLL | 442 | 777 | 57% |

Table 3.4: statistical data for the cross-match BZCat vs. GLEAM. We have not data for SED and spectroscopic classifications.

| class | number matches | number sources | detection rate |
|---|---|---|---|
| total | 530 | 747 | 71% |
| FSRQ | 239 | 267 | 90% |
| BCU | 40 | 214 | 19% |
| BLL | 248 | 257 | 96% |
| LSP | 331 | 424 | 78% |
| ISP | 88 | 131 | 67% |
| HSP | 106 | 165 | 64% |

Table 3.5: statistical data for the cross-match 3LAC-GLEAM vs. BZCat-GLEAM

| class | number matches | number sources | detection rate |
|---|---|---|---|
| total | 2906 | 11112 | 26% |

Table 3.6: statistical data for the cross-match SDSS-FIRST-NVSS vs. GLEAM. We have not data for SED and spectroscopic classifications.

| class | number matches | number sources | detection rate |
|---|---|---|---|
| total | 367 | 747 | 49% |

Table 3.7: statistical data for the cross-match 3LAC-GLEAM vs. 3LAC-AT20G. We have not data for SED and spectroscopic classifications.

# Chapter 4

# Results about the spectral properties for blazars detected at low frequency

## 4.1 Detection rate: a jump from MWACS to GLEAM

In the previous chapter we reported on a previous work (Giroletti et al. 2016) where some gamma-ray blazars are detected at low frequency with MWACS. With the GLEAM the detection rate grows to 78%, compared to 45% found in MWACS. Also the detection rate grows for every kind of objects, both considering the SED and spectroscopic classification. The growth of the detection rate is impressive, in particular for the faintest classes, such as BL Lacs, which raises from 22% in MWACS to 71% in GLEAM. However, the largest group of sources remains that of LSP, both because there are many of them in the starting sample (3LAC) and because the detection rate is larger. We reported the results in the Table 4.1. We see that the number of the LSP is larger than the number of the ISP and the HSP. Infact, the former have the largest detection rate for the SED classification. Also the

number of the ISP is lower than the number of the HSP, but the latter have a lower detection rate. For the spectroscopic classification the FSRQs have the largest detection rate, instead the detection rates for the BL Lacs and the BCUs are similar. The Figures 4.1 and 4.2 give us an idea about the detection rate as a function of the $\sim$ GHz flux density (Fig. 4.1) and the gamma-ray energy flux (Fig. 4.2). Infact in these figures we compared the 3LAC sample with the GLEAM sample. We can see that the detection rate grows for brighter objects, both in the radio band and in the gamma band. The two distributions do not have the exact same shape. The starting gamma-ray energy distribution has the typical features of the source count distribution for a complete sample: the source counts increase regularly as the flux decreases, and then they suddenly turn over as the limiting sensitivity is reached; the brightest gamma-ray sources nearly always have a GLEAM match, and then the GLEAM detection rate decreases for fainter sources.

The radio distributions are much more symmetric, without a well defined turn over at low flux density. An interesting feature is the rather large number of gamma-ray blazars with GHz radio flux density larger than the GLEAM sensitivity (6-10 mJy) but not detected in our match. These sources must have an inverted spectrum.

### 4.1.1 Multi-wavelength and spectral statistical properties

In this section we report the results about the values for the mean flux (in X, gamma and radio band) and the spectral index. So we show the spectral properties through the numbers. We reported the mean values in the Table 4.2. We can see some properties that we will discuss also in the next section: in the radio band the LSP are brighter than the HSP, while in the X-ray band the latter are brighter than the former. In the gamma band we have the same behaviour of the radio band for the HSP and LSP. Instead, the ISP have intermediate value of the flux in every band. Also the FSRQs are

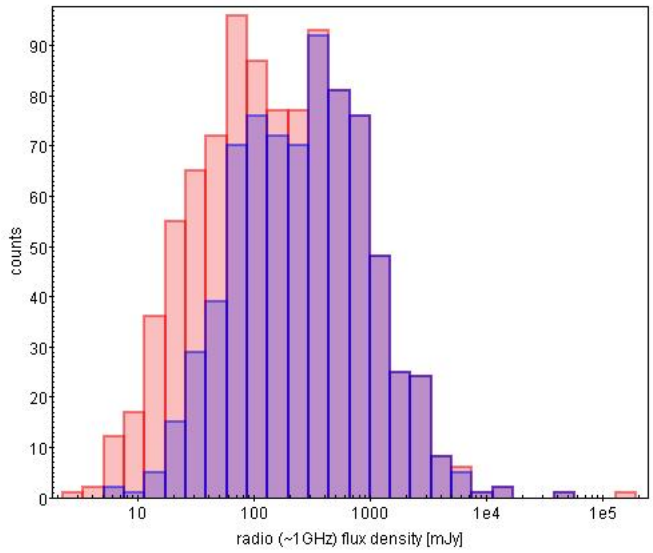


Figure 4.1: radio flux density at 1GHz distribution for the entire 3LAC sample (red) in the GLEAM sky and 3LAC sources with a GLEAM counterpart (blue).

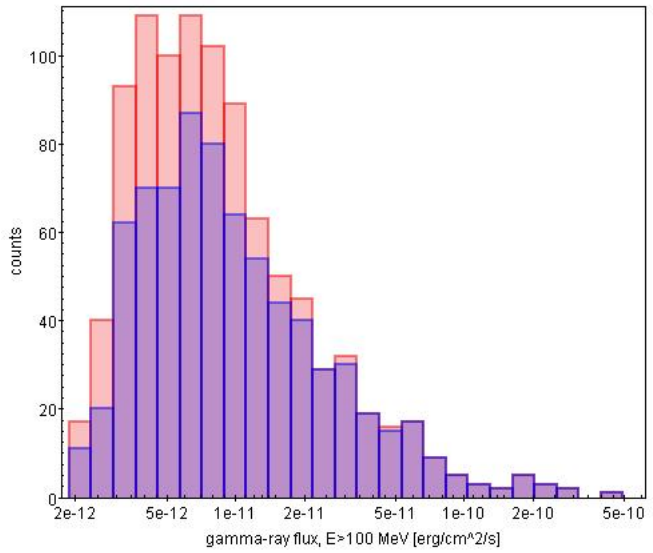


Figure 4.2: gamma-ray flux at E > 100 MeV distribution for the entire 3LAC sample (red) in the GLEAM sky and 3LAC sources with a GLEAM counterpart (blue).

| class | ratio | detection rate for GLEAM | ratio | detection rate for MWACS |
|---|---|---|---|---|
| total | 747/963 | 78% | 87/247 | 35% |
| FSRQ | 267/278 | 96% | 52/71 | 73% |
| BCU | 214/312 | 69% | 16/89 | 18% |
| BLL | 257/362 | 71% | 19/87 | 22% |
| LSP | 424/460 | 92% | 67/128 | 52% |
| ISP | 131/179 | 73% | 11/37 | 30% |
| HSP | 165/270 | 61% | 9/68 | 13% |

Table 4.1: The detection rate from MWACS to GLEAM grows for every kind of object.

brighter than the BL Lacs in the radio and gamma band. In the X-ray band the BL Lacs are brighter than the FSRQs. In the radio and X-ray band the BCUs have intermediate value of the flux; instead in the gamma band they are the objects with the lowest flux. The Figure 4.3 is a flux density distribution at low frequency, and show that blazars are brighter than the rest of GLEAM sources.

Moreover we reported in the Table 4.3 the mean values of the spectral index. We note that the GLEAM catalogue does not report a spectral index for all sources, since some of them have complex spectra difficult to fit with a power law. Therefore, we write the total number of sources (detected at low frequency) and the number of the sources with the value for spectral index for every class. Analyzing the values of the spectral index, we see that the LSP seem have a slightly flatter spectrum than the HSP ($\Delta\alpha = \alpha_{\rm LSP} - \alpha_{\rm HSP} = 0.23$). So, at first sight, the LSP are closer to a core dominated object and they are closer to a lobe dominated object. This is an intriguing result. Infact, before we expected every blazar to have about the same value of the spectral index, instead now we see different values for HSP and LSP. Also we observe a similar difference between BL Lacs and FSRQs, yet quantitatively less significant ($\Delta\alpha = 0.06$).

Moreover, the mean value of the spectral index for all objects in the GLEAM is $< \alpha >= -0.77$, while the value for the object reported both in the GLEAM and in the 3LAC is $< \alpha >= -0.45$. Also we reported a distribution for the spectral index (Fig. 4.4) that show this behaviour. This result is of great interest: while it is well known that blazars have flat spectra at high frequency, it has only recently started to become clear that they maintain a flat spectrum down to low frequency (Massaro et al. 2013, Nori et al. 2014). Our result indicates that the flat spectrum cores still contribute a substantial fraction of the radio emission in the $\sim$ 100 MHz regime. We will estimate this fraction in a later section of this work. This distribution is an interesting test for the Unified Model for AGN. Infact for this model the objects with a larger spectral index are core dominated and the objects with a lower spectral index are lobe dominated.

| class | log $F_{\rm rad}$ [mJy] | log $F_{\rm X}$ [$10^{-13} erg/cm^2/s$] | log $F_\gamma$ [erg/cm$^2$/s] |
|---|---|---|---|
| total | 2.4 $\pm$0.6 | 1.5 $\pm$0.6 | -11.0 $\pm$0.4 |
| FSRQ | 2.8 $\pm$0.4 | 1.2 $\pm$0.4 | -10.9 $\pm$0.4 |
| BCU | 2.2 $\pm$0.5 | 1.4 $\pm$0.5 | -11.2 $\pm$0.3 |
| BLL | 2.2 $\pm$0.5 | 1.7 $\pm$0.6 | -11.0 $\pm$0.4 |
| LSP | 2.7 $\pm$0.5 | 1.2 $\pm$0.4 | -10.9 $\pm$0.4 |
| ISP | 2.3 $\pm$0.5 | 1.2 $\pm$0.4 | -11.1 $\pm$0.4 |
| HSP | 1.9 $\pm$0.4 | 1.8 $\pm$0.5 | -11.1 $\pm$0.4 |

Table 4.2: values for the logarithm of the radio ($\sim$ 1GHz) flux density $F_{\rm rad}$, X-ray flux $F_{\rm X}$ and gamma-ray flux $F_\gamma$. The associated errors are the standard deviations.

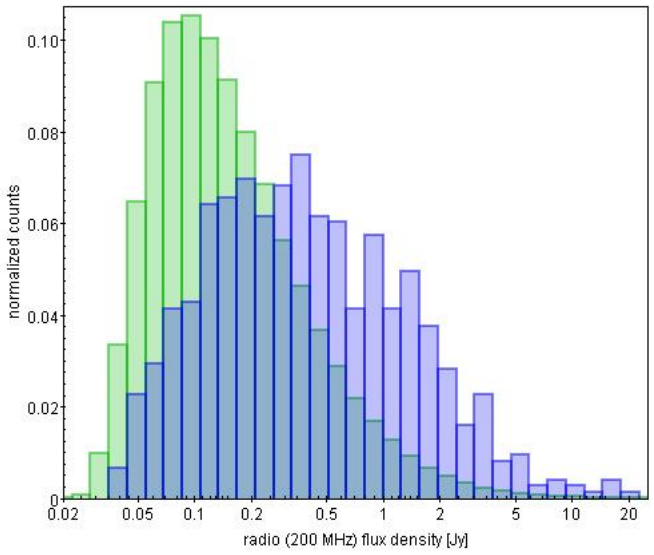


Figure 4.3: normalized flux density distribution at low frequency for all GLEAM sources (green) and low frequency detected blazars (blue). Blazars are brighter then the rest of GLEAM sources.

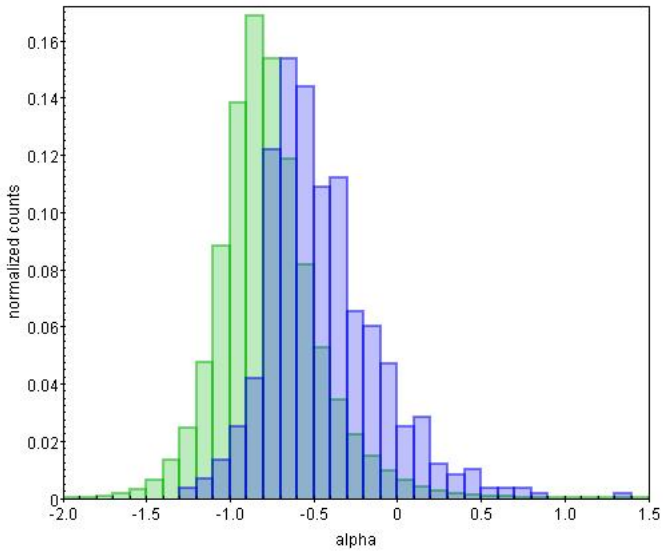


Figure 4.4: normalized spectral index distribution for the blazars detected at low frequency (blue) and all GLEAM sources (green). The blazars are flatter-spectrum objects than the rest of the sample.

| class | total sources | sources with $\alpha$ | $\langle\alpha_{\rm GLEAM}\rangle \pm \sigma_{\alpha{\rm GLEAM}}$ |
|---|---|---|---|
| total | 747 | 598 | -0.45 ±0.34 |
| FSRQ | 267 | 226 | -0.39 ±0.33 |
| BCU | 214 | 173 | -0.51 ±0.36 |
| BLL | 257 | 192 | -0.45 ±0.30 |
| LSP | 424 | 354 | -0.34 ±0.35 |
| ISP | 131 | 103 | -0.50 ±0.32 |
| HSP | 165 | 123 | -0.57 ±0.27 |

Table 4.3: mean values for the spectral index with the total number of blazars detected at low frequency and the number of sources with a value of the spectral index $\alpha$. The associated errors are the standard deviation.

## 4.2 Multi-wavelength properties

We analyzed the multi-wavelength properties of all blazars detected at low frequency, and in this section we report the results.

We observed a strong correlation between the radio emission at low frequency (GLEAM data) and the radio emission at intermediate frequency (3LAC data). All kinds of sources present this correlation, and it is very strong because the correlation coefficient r is very close to 1 (r=0.85). We reported the values of the correlation coefficient for the populations of the sample in the table 4.4.

Also we must specify for intermediate frequency we refer a close frequency to about 1 GHz. Infact the radio data at intermediate frequency come from the 3LAC, and the radio data of this catalog come from many catalogues: NVSS, AT20G, SUMSS, PMN. So the most data are close to 1 GHz. Instead, the radio data at low frequency come from the GLEAM, and are at 200 MHz.

Another interesting correlation is the relation between the gamma emission and the radio emission (both at low and intermediate frequency). The

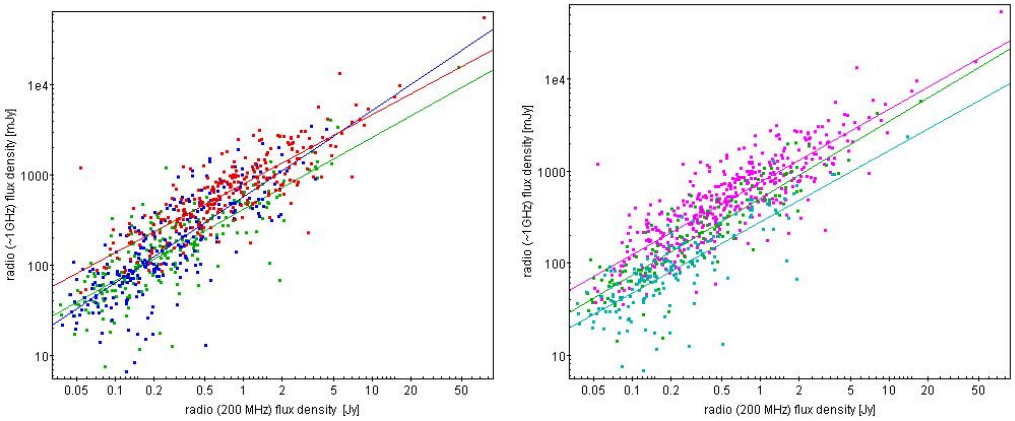


Figure 4.5: correlation between radio emission at low frequency and radio emission at intermediate frequency. Spectroscopic classification (left): FSRQs (red), BLL (blue), BCU (green). SED classification (right): LSP (magenta), ISP (green), HSP (cyan). The solid lines show best fit regression.

correlation is present for every population of the sample, but with different degrees of strenght and significance, and in general much weaker than that between the two radio frequencies.

The correlation between gamma emission and radio emission is stronger with the radio flux density at 1 GHz because the gamma emission and radio emission at intermediate frequency are beamed, while the radio emission at low frequency is not beamed. Infact we see the core emission at intermediate frequency and the extended emission at low frequency.
Moreover, both low and intermediate frequency, we can see a slight different placement between LSP and HSP. Infact, the LSP have a larger flux emission in the gamma band and in the radio band. However this behaviour is not evident, infact there is scatter of the points in the plots gamma-ray energy flux vs. radio flux density. Also, we can see a similar behaviour for the FSRQs and the BL Lacs. In other words, the LSP and the FSRQs are brighter. Infact the most sources in the GLEAM catalog are LSP and FSRQs.

The flux densities are observed quantities but the intrinsic property of in-

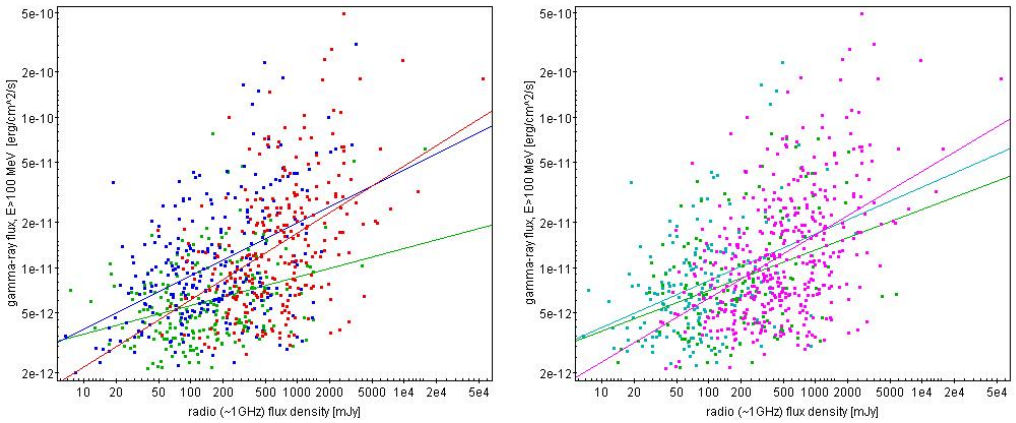


Figure 4.6: correlation between gamma emission and radio emission at intermediate frequency. Spectroscopic classification (left): FSRQ (red), BL Lac (blue), BCU (green). SED classification (right): LSP (magenta), ISP (green), HSP (cyan).

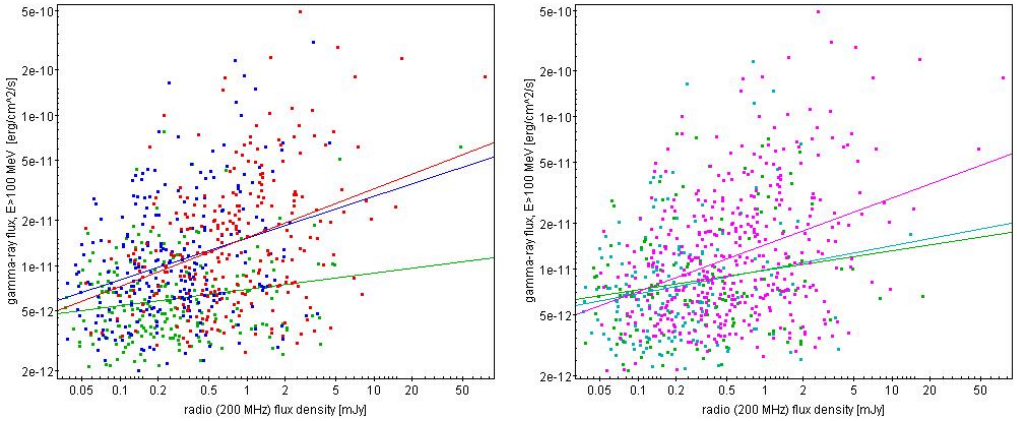


Figure 4.7: correlation between gamma emission and radio emission at low frequency. Spectroscopic classification (left): FSRQ (red), BL Lac (blue), BCU (green). SED classification (right): LSP (magenta), ISP (green), HSP (cyan).

| class | $r$ |
|---|---|
| total | 0.85 |
| FSRQ | 0.85 |
| BCU | 0.82 |
| BLL | 0.80 |
| LSP | 0.85 |
| ISP | 0.89 |
| HSP | 0.79 |

Table 4.4: values for the correlation coefficient $r$ for the correlation between radio emission at intermediate frequency and radio emission at low frequency.

terest is the luminosity. In Chapter 2, we showed the redshift distribution for the entire 3LAC, and here we consider the same distribution for the sources with a GLEAM counterpart. In particular, we have a segregation, which is well visible in Fig. 4.8. Infact the HSP and the BL Lacs are at low redshift while the LSP and the FSRQs are at high redshift. So the LSP and FSRQs have a larger intrinsacally luminosity.

Also we studied the relation between X-ray emission and radio emission (Fig. 4.9). We see the region of the graphic occupied by FSRQs is on bottom right. So the FSRQs are the objects with lowest X-ray emission and larger radio emission. Instead, the other sources (BL Lacs and BCUs) can have high or low X-ray emission and they can have high or low radio emission, but a single BL Lac or BCU cannot have both high X-ray emission and high radio emission (except few cases). In other words, the upper right region is not occupied by sources. Moreover we must report that there are 431 objects with a negligible X-ray emission and we do not consider these sources in every plot with the X-ray emission. We have 316 objects with a considerable X-ray emission.

Instead, for the LSP, ISP and HSP there is a segregation between LSP

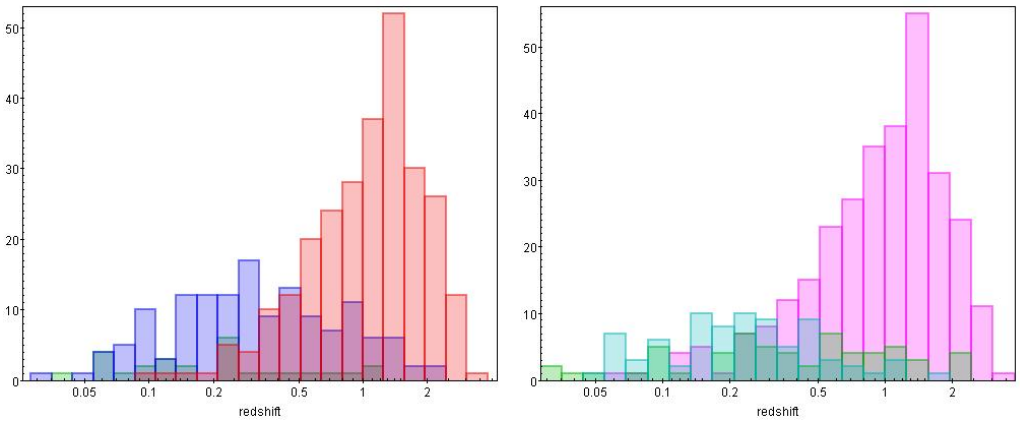


Figure 4.8: redshift distribution. Spectroscopic classification (left): FSRQs (red), BCUs (green), BL Lacs (blue). SED classification (right): LSP (magenta), ISP (green), HSP (cyan).

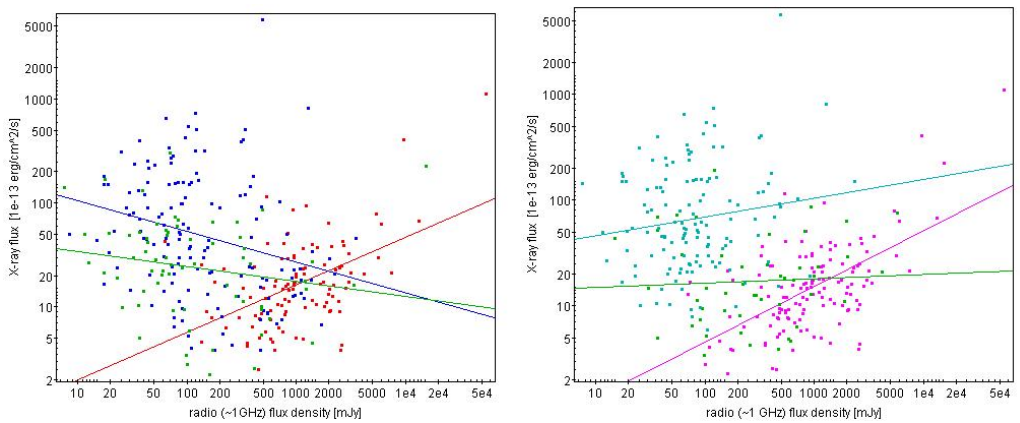


Figure 4.9: Plot of X-ray flux vs. radio density flux. Spectroscopic classification (left): FSRQs (red), BL Lacs (blue), BCUs (green). SED classification (right): LSP (magenta), ISP (green), HSP (cyan).

| class | $r$ |
|---|---|
| total | 0.47 |
| FSRQ | 0.46 |
| BCU | 0.33 |
| BLL | 0.45 |
| LSP | 0.47 |
| ISP | 0.36 |
| HSP | 0.37 |

Table 4.5: values for the correlation coefficient $r$ for the correlation between gamma emission and radio emission at intermediate frequency.

and HSP: the latter have larger X-ray emission but they have lower radio emission. For the LSP it is true the opposite. While the ISP have larger scatter in the graphic.

We just plotted the two graphics with radio flux density at intermediate frequency, but the behaviour is similar at low frequency. Also there is not a correlation between X-ray emission and radio emission for BL Lacs, BCUs, HSP and ISP. Instead we see a correlation for the LSP and FSRQs. We reported the value coefficient correlation for every population in Table 4.7. For this reason, the linear fits in Fig. 4.9 are only meaningful for FSRQ and LSP, while they have very little significance for the other sub-classes.

Moreover we looked for a relation between gamma ray emission and X-ray emission. In particular, we do not see a correlation for all sources, but for the LSP, HSP and FSRQs the value coefficient correlation is not negligible.

Also we examined the position of the synchrotron peak versus the photon index. We noticed a strong anticorrelation. We see a segregation between FSRQs and BL Lacs. In particular the FSRQs have a larger photon index and the synchrotron peak is at lower frequency than the BL Lacs. However, there are some BL Lacs with values, for the photon index and the frequency of the synchrotron peak, similar to the FSRQs. Moreover, there are BCUs

| class | $r$ |
|---|---|
| total | 0.35 |
| FSRQ | 0.37 |
| BCU | 0.20 |
| BLL | 0.30 |
| LSP | 0.37 |
| ISP | 0.19 |
| HSP | 0.19 |

Table 4.6: values for the correlation coefficient $r$ for the correlation between gamma emission and radio emission at low frequency.

both in the region occupied by the FSRQs and the region occupied by the BL Lacs. By definition, for the SED classification the segregation is more evident about the position of the peak. Also there is a segregation for the photon index: the LSP have a larger photon index than the HSP. The ISP occupy an intermediate position in the plot.

We see another anticorrelation for the plot with the gamma luminosity and the photon index. In the previous plot we seen that the FSRQs and the LSP are the objects with the largest photon index. In this plot we see the same behaviour. Also the FSRQs and the LSP present the largest value for the gamma luminosity. The BCUs and the LSP can have both large and low values for the gamma luminosity and the photon index.

We studied the behaviour of the gamma luminosity with the redshift, and we see the LSP and the FSRQs have larger gamma luminosity and are at larger redshift than the HSP and the BL Lacs. So the gamma emission grows with the redshift. However we must consider that the detection limit grows with the redshift, so we cannot observe some objects with low gamma luminosity at high redshift. This effect is the Malmquist bias.

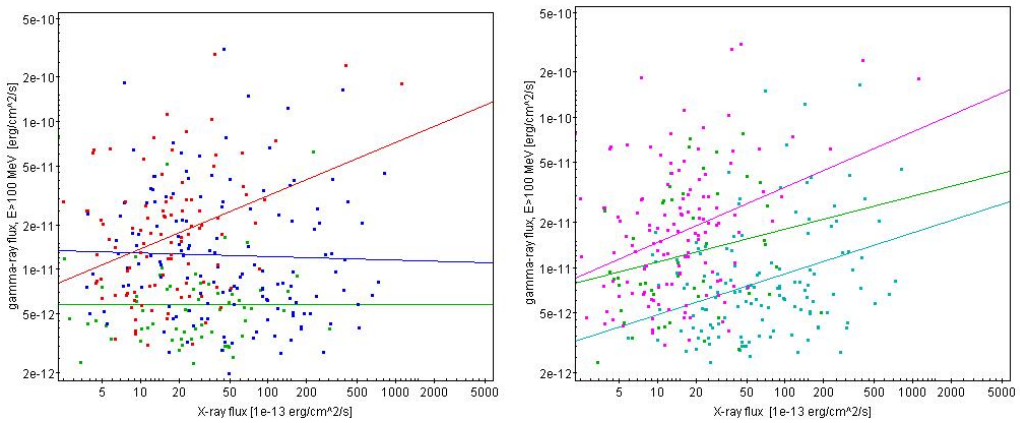


Figure 4.10: Plot of gamma-ray flux vs. X-ray flux. Spectroscopic classification (left): FSRQs (red), BL Lacs (blue), BCU (green). SED classification (right): LSP (magenta), ISP (green), HSP (cyan).

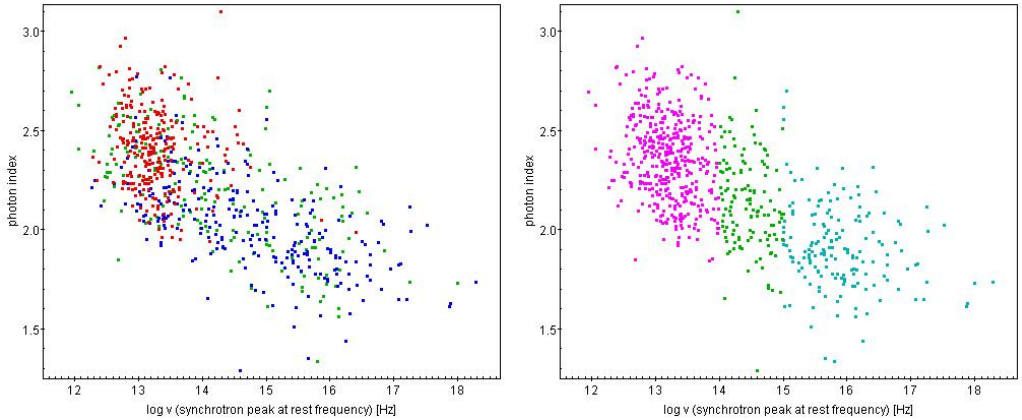


Figure 4.11: photon index vs. synchrotron peak. Spectroscopic classification (left): FSRQs (red), BL Lacs (blue), BCUs (green). SED classification (right): LSP (magenta), ISP (green), HSP (cyan).

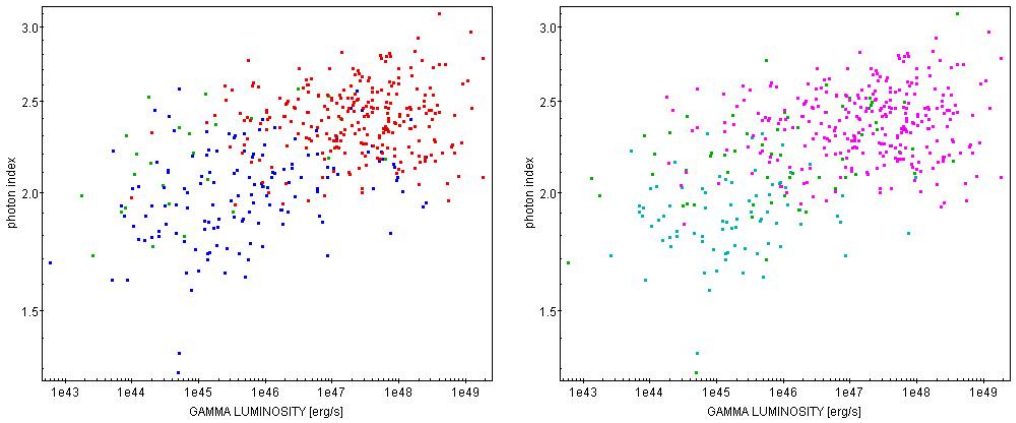


Figure 4.12: photon index vs. gamma luminosity. Spectroscopic classification (left): FSRQs (red), BL Lacs (blue), BCUs (green). SED classification (right): LSP (magenta), ISP (green), HSP (cyan).

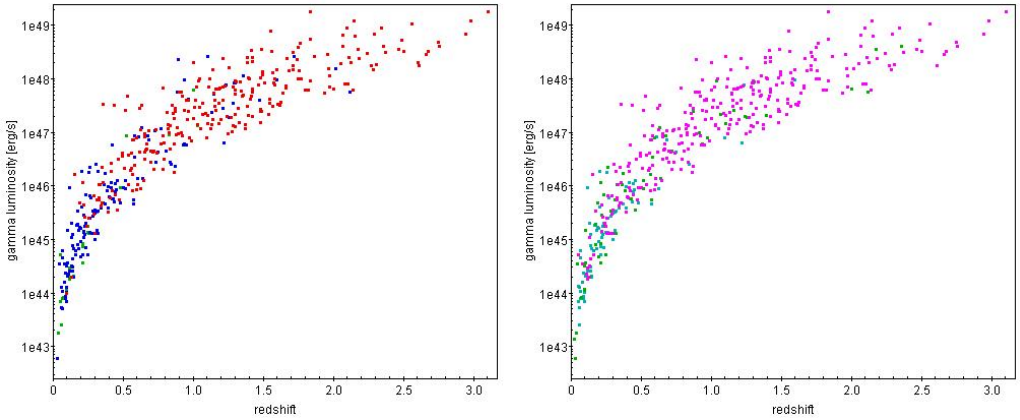


Figure 4.13: gamma luminosity vs. redshift. Spectroscopic classification (left): FSRQs (red), BL Lacs (blue), BCUs (green). SED classification (right): LSP (magenta), ISP (green), HSP (cyan).

| class | $r$ |
|---|---|
| total | -0.23 |
| FSRQ | 0.49 |
| BCU | -0.19 |
| BLL | -0.27 |
| LSP | 0.59 |
| ISP | 0.05 |
| HSP | 0.15 |

Table 4.7: values for the correlation coefficient $r$ for the plot X emission vs. radio emission at intermediate frequency.

## 4.3 Discussion about the FSRQs and LSP

Many FSRQs are LSP objects. We can to do this conclusion because we have many results that suggest this correspondence:

1)overloap between the FSRQs and the LSP in every plot with gamma-ray flux, X-ray flux, radio flux density, gamma luminosity, photon number, redshift and synchrotron peak.

2)the redshift distribution show that the FSRQs and the LSP are the objects with larger redshift and these values coincide in many cases, in particular the most sources are close to z=2;

3)the detection rate for the two populations are similar ( 92% for the FSRQs and 96% for the LSP);

4)similar value for the spectral index for the two populations.

We verified the corrispondece: we cross-correlated the two samples and

| class | $r$ |
|---|---|
| total | 0.05 |
| FSRQ | 0.35 |
| BCU | -0.002 |
| BLL | -0.03 |
| LSP | 0.34 |
| ISP | 0.22 |
| HSP | 0.35 |

Table 4.8: values for the correlation coefficient $r$ for the plot gamma emission vs. X emission.

we obtained 238 matches and we know that the LSP are 424 but the FSRQs are 267, so the most FSRQs are LSP (about 89%).

## 4.4 Discussion about the BL Lacs and HSP

An important fraction of the BL Lacs and the HSP have similar properties:

1)in every plot we have an important overloap between the BL Lacs and the HSP, but many BL Lacs are also in the regions employed by ISP and LSP;

2)they are the objects with lowest redshift.

We cross-matched the two samples: the HSP are 165, the BL Lacs are 257, and we obtained 104 matches, so about 40% of the BL Lacs are HSP.

## 4.5 Summary of the spectral properties

In this section we show a summary of the spectral properties:

1)the FSRQs and the LSP are the objects with a largest gamma-ray emission and radio emission, while the BL Lacs and the HSP are the the objects with a lowest emission in these two bands;

2)the BL Lacs and the HSP are the the objects with a largest X-ray emission unlike the FSRQs and the LSP, infact the latter have a lower emission in this band;

3)the FSRQs and the LSP are at high redshift (especially about z=2), while the BL Lacs and the HSP are at low redshift;

4)the FSRQs and the LSP are the objects with a largest photon number, for the the BL Lacs and the HSP is true the opposite;

5)the FSRQs and the LSP have the synchrotron peak at low frequency, unlike the BL Lacs and the HSP;

6)the FSRQs and the LSP are the objects with a largest spectral index, for the the BL Lacs and the HSP is true the opposite,so the former are closer to a core dominated source and the latter are closer to a lobe dominated source.

However for the BL Lacs the segregation with the FSRQs and the LSP are not so strong, infact only a fraction of the BL Lacs are HSP. Instead almost all FSRQs are LSP. The BCU and the ISP have intermediate properties between the four populations.

The value of the spectral index for the HSP is $< \alpha >= 0.57$ while for

the LSP is $< \alpha >= 0.34$. Before now we considered the blazars like object with the same value for the spectral index, instead now we see different value for two class of the blazars. Since the two populations have also different redshift distributions, it is also possible that this difference is due to the fact that we are probing different parts of the rest-frame spectrum.

In general, we confirm the spectral properties observed in the previous work (Giroletti et al. 2016), where the authors cross-correlated the 3LAC with the MWACS, while we used the GLEAM and not the MWACS. Given the much larger number of sources considered (747 vs. 87, i.e. an impressive 860% improvement), the results now have a much higher statistical significance. In particular, this holds for BL Lacs and HSP sources, which were severely underrepresented in the MWACS sample.

## 4.6 A further study of the spectral properties of gamma-ray blazars

We used the Roma BZCat to execute a further study of gamma-ray blazars. In particular we used the cross-correlation BZCat-GLEAM vs. 3LAC-GLEAM to obtain a sample composed by blazars reported both in the BZCat and in the 3LAC. Infact the latter only contains gamma-ray blazars, instead the former contains every kind of blazars (we remember that the BZCat is the most complete catalog for blazars). Also all sources of the cross-correlation are detected at low frequency and they are reported in the GLEAM catalog. We examined the spectral properties of the objects selected and we obtained similar results respect the study with the 3LAC and the GLEAM.

Moreover, we studied the data of the anticross-correlation BZCat-GLEAM vs. 3LAC-GLEAM and the data of the cross-correlation of the same samples, to compare the spectral properties of blazars without important emission in the gamma band with gamma-ray blazars. We reported the results in the

Tables 4.9 and 4.10. We see that the gamma-ray blazars have a larger radio emission than the other blazars. Also, analyzing the spectral index the former have a flatter spectrum than the latter. These properties are true for every kind of objects (spectroscopic classification). Moreover we see a larger number of gamma-ray blazars at low redshift, infact the mean redshift for these souces are lower than the other blazars. We have this result because the *Fermi* satellite has not a large sensitivity (the technical features are reported in the Tables 2.9 and 2.10) and the faraway and very luminous objects have peaks of emission at lower energies respect to the *Fermi* band. For the BL Lacs it is true the opposite but we must consider many BL Lacs have not a value for the redshift. Infact these objects have weak lines in the spectrum and it is difficult to determine the right value for the redshift.

| class | log $F_{\rm rad}$ [mJy] | $<\alpha>$ | $<z>$ |
|---|---|---|---|
| total | 2.52 | -0.40 | 0.71 |
| FSRQ | 2.84 | -0.36 | 1.22 |
| BCU | 2.53 | -0.36 | 0.50 |
| BLL | 2.22 | -0.44 | 0.26 |

Table 4.9: results for gamma-ray blazars (data of the cross-correlation BZCat-GLEAM vs. 3LAC-GLEAM).

| class | log $F_{\rm rad}$ [mJy] | $<\alpha>$ | $<z>$ |
|---|---|---|---|
| total | 2.40 | -0.44 | 1.19 |
| FSRQ | 2.48 | -0.41 | 1.48 |
| BCU | 2.43 | -0.53 | 0.65 |
| BLL | 2.01 | -0.56 | 0.17 |

Table 4.10: results for blazars without an important emission in the gamma band (data of the anticross-correlation BZCat-GLEAM vs. 3LAC-GLEAM).

# Chapter 5

# Results about the radio cores and the lobes for radio loud AGN

## 5.1 Correlation between gamma-rays and high frequency radio emission

In this chapter we report the results for the radio core of radio sources. To study the properties of the core, we used a survey at high frequency: the AT20G. In Chapter 4 we showed the correlation gamma emission vs. radio emission at low and intermediate frequency. Also we saw that the correlation is stronger at intermediate frequency. This phenomenon is caused by the beaming effect. In this section we show this effect is more evident at high frequency. In other words, increasing the radio frequency, the beaming effect is more evident. We reported the correlation in the Fig. 5.1. Also we reported the values for the correlation coefficient in the Table 5.1.

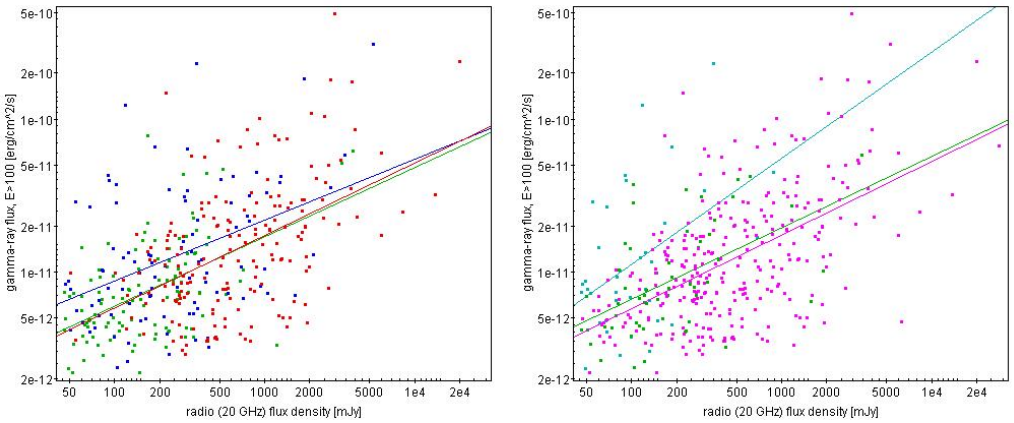


Figure 5.1: gamma emission vs. radio emission at high frequency. Spectroscopic classification (left): FSRQs (red), BL Lacs (blue), BCUs (green). SED classification (right): LSP (magenta), ISP (green), HSP (cyan).

## 5.2 A test for the Unified Model of AGN: the core dominance

At higher radio frequency we see the emission from the core of every sources, while at lower frequency we see the extended emission. We saw that the core emission is increased due to the beaming effect. Therefore the ratio between the core emission and the extended emission is increased due to this effect. We used the sample originated with the cross-correlation GLEAM-AT20G (4271 sources) to plot the GLEAM spectral index versus the ratio between the core flux density (estimated from the sub-arcsecond scale AT20G flux density at 20 GHz) and the lobe emission (estimated from the arcminute scale GLEAM flux density measured at 200 MHz). We expected that core dominated objects have a flatter spectral index. Instead, for lobe dominated objects had to be true the opposite. Infact we observe this behaviour for the plot (Fig. 5.2). There is a scatter effect but we see a relation with a correlation coefficient $r = 0.43$.

The objective of this work is to estimate the ratio between the core power

| class | $r$ |
|---|---|
| total | 0.52 |
| FSRQ | 0.49 |
| BCU | 0.52 |
| BLL | 0.42 |
| LSP | 0.55 |
| ISP | 0.53 |
| HSP | 0.46 |

Table 5.1: values for the correlation coefficient $r$ for the plot gamma emission vs. radio emission at high frequency.

| class | $r$ |
|---|---|
| total | 0.43 |

Table 5.2: value for the correlation coefficient $r$ for the correlation spectral index vs. ratio between flux density at 20 GHz (core emission) and flux density at 200 MHz (extended emission).

and the total power (defined as "*core dominance*") and to examine the behaviour with the GLEAM spectral index. The purpose would be to use the GLEAM spectral index, which is available for a huge number of sources all over the sky, as a proxy of the core dominance and, in turn, of the Doppler beaming. While for any single object this will have a large uncertainty, we are interested in understanding how this could be done in a statistical sense. We expected a similar behaviour compared to the plot with the flux density ratio. To estimate the power for the core and the extended region we used the relation (5.1), where $P$ is the power and $D$ is the luminosity distance.

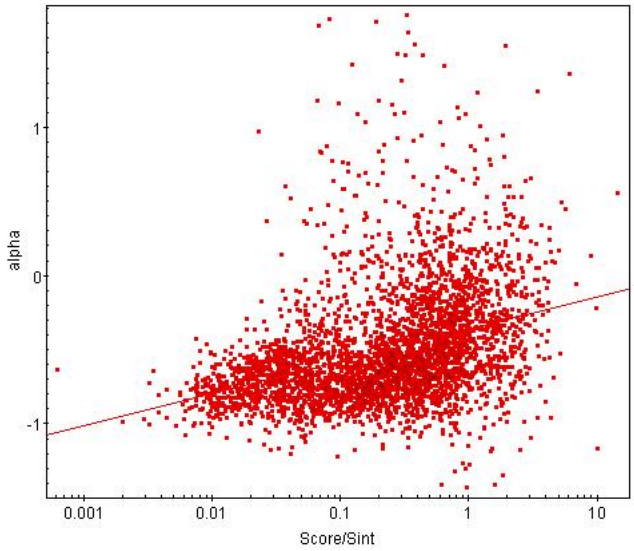


Figure 5.2: GLEAM spectral index vs. ratio between flux density at 20 GHz (core emission) and flux density at 200 MHz (extended emission).

$$P = 4\pi S D^2 \quad (5.1)$$

The core dominance is estimated in Giovannini et al. 1988, where the authors studied a sample composed by 187 radio galaxies. So we compared their sample with our much larger sample. The latter is originated by the cross-correlation AT20G-GLEAM (4271 objects) but we plotted 1331 sources, infact for the other objects we do not know the redshift and the luminosity distance, so it is not possible to estimate the core power and the total power. However, our sample is still almost of one order of magnitude larger than the sample in Giovannini et al. 1988. We plotted the two samples in the plane core power versus total power. For our sample the core power is at 20 GHz, instead for the sample of Giovannini et al. 1988 it is at 5 GHz. We can safely assume that the core has a flat spectrum ($\alpha = 0$); moreover, we obtained total power at 408 MHz (as used by Giovannini et al 1988) extrapolating the 200 MHz flux densities with the GLEAM spectral index.

We see a correlation for both our sample and the sample of Giovannini

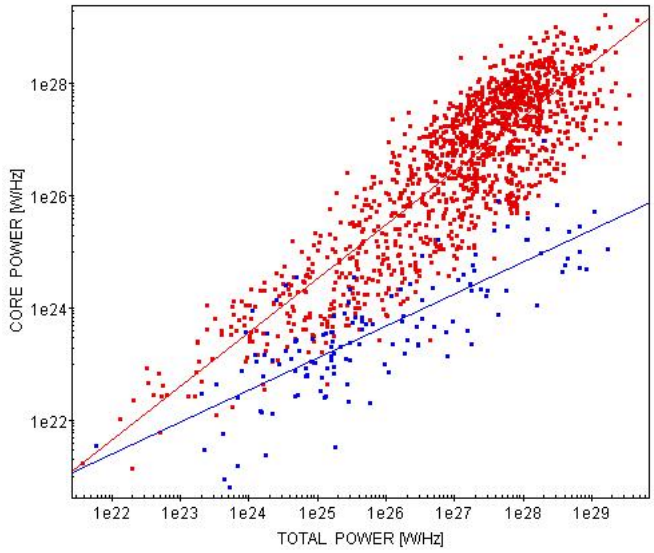


Figure 5.3: core power vs. total power for the sample AT20G-GLEAM (red) and the sample of Giovannini et al. 1988 (blue).

et al. 1988, but there is a deviation between the two samples. Infact our objects have a larger core emission. It is evident that the our sample is not representative to describe the entire population of AGN. The AT20G must have only the brightest and most core dominated sources and not the other objects. This idea is confirmed by the larger sources density in the upper region of the graphic. Also, we reported the values for the correlation coefficient and the values for the angular coefficient in the Table 5.3. The difference $\Delta m = 0.96 - 0.57 = 0.39$ between the two values of the angular coefficient describe the deviation between the samples.

| sample | $r$ | $m$ |
|---|---|---|
| AT20G-GLEAM | 0.86 | 0.96 |
| Giovannini et al. 1988 | 0.80 | 0.57 |

Table 5.3: values for the correlation coefficient $r$ and the angular coefficient $m$ for the samples AT20G-GLEAM and Giovannini et al. 1988 for the plot core power vs. total power.

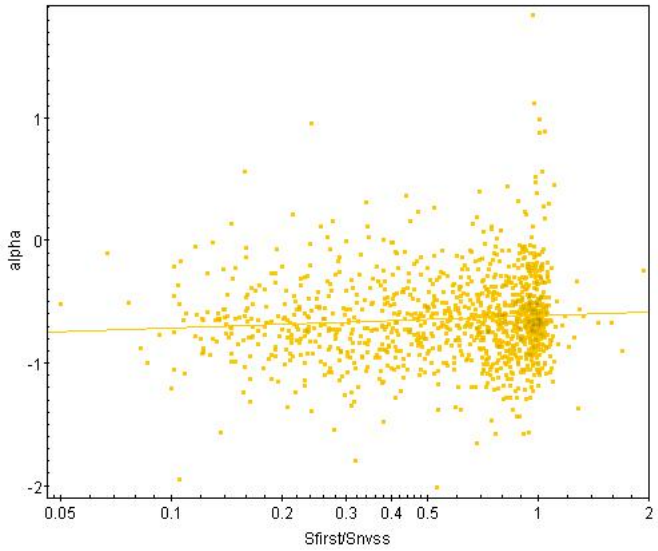


Figure 5.4: spectral index vs. ratio between flux density of FIRST (core emission) and flux density of NVSS (extended emission).

Therefore we used the sample generated by the cross-correlation between the sample SDSS-FIRST-NVSS and the sample GLEAM (see Sect. 3.8). We estimated the ratio between the flux density of FIRST and the flux density of NVSS. Both catalogues have a flux density at 1.4 GHz but the angular resolution of FIRST (5 arcsec) is better than the angular resolution of NVSS (45 arcsec). So the FIRST must favor the core emission while the NVSS must favor the extended emission. We plotted the spectral index versus the ratio flux density (Fig. 5.4).

We plotted 1713 sources while the entire sample contains 2906 objects. Infact we just plotted the objects with a counterpart for the FIRST and for the NVSS. Instead, the other objects have more than one counterpart for NVSS or FIRST or they have not a value for the flux density of the FIRST. Also we define as $S_F$ the flux density of the FIRST and as $S_N$ the flux density of the NVSS. We expected that core dominated objects have a ratio $S_F/S_N \sim 1$ and lobe dominated objects have a ratio $S_F/S_N < 1$. We observe a larger sources density close to the ratio $S_F/S_N = 1$ and for the

same value for the ratio there is an important scatter for the spectral index. Also, we do not see a clear correlation ($r = 0.08$).

| class | $r$ |
|---|---|
| total | 0.08 |

Table 5.4: value for the correlation coefficient $r$ for the plot spectral index vs. ratio between flux density of FIRST (core emission) and flux density of NVSS (extended emission).

Therefore we divided the sample in four subsets: from the first subset to the fourth subset the mean ratio $< S_F/S_N >$ decreases. We expected the mean spectral index $< \alpha >$ decreases from the first to the fourth subset. Every subset have about 428 objects (we remember the entire sample is composed by 1713 sources).

| sample | $< \alpha >$ | SD | <Sfirst/Snvss> |
|---|---|---|---|
| first subset | -0.57 | 0.38 | 1.03 |
| second subset | -0.64 | 0.34 | 0.86 |
| third subset | -0.64 | 0.33 | 0.58 |
| quarter subset | -0.68 | 0.35 | 0.24 |

Table 5.5: results about the mean spectral index and the flux density ratio. In the third column there is the error (standard deviation) for the mean spectral index.

We see the mean spectral index of the first subset is larger than the fourth subset. The difference is however very small ($\Delta\alpha = -0.57 + 0.68 = 0.11$), indicating that the effect is diluted by other possible causes.
Moreover, we plotted the core power versus the total power. Both the powers are estimated using the relation (5.1). To calculate the core power we used the flux density of the FIRST, instead for the total power we used the flux density of the GLEAM estimated at 408 MHz. Also we plotted the sample

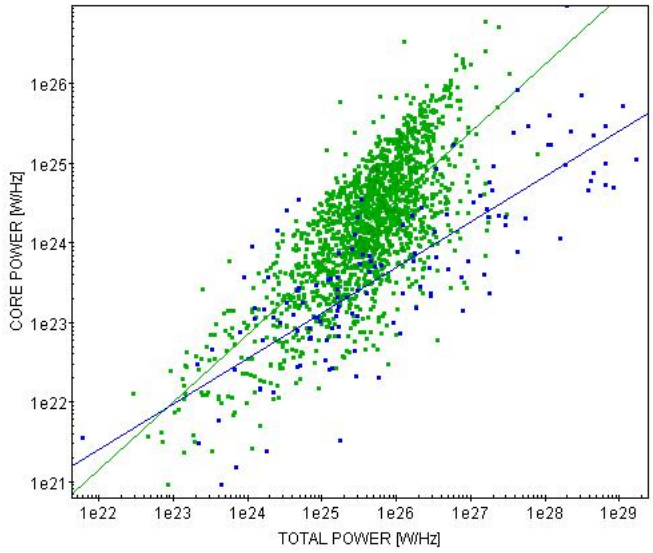


Figure 5.5: core power vs. total power for the sample SDSS-FIRST-NVSS (green) and the sample of Giovannini et al. 1988 (blue).

with the sample of Giovannini et al. 1988. So we applied the same operation executed with the AT20G. Even in this case we see a deviation between the two samples. The objects of the sample SDSS-FIRST-NVSS-GLEAM have a larger core power. We reported the values of the correlation coefficients and of the angular coefficient. The difference between the two angular coefficients describes the deviation: $\Delta m = 0.85 - 0.57 = 0.28$.

| sample | $r$ | $m$ |
|---|---|---|
| SDSS-NVSS-FIRST-GLEAM | 0.74 | 0.85 |
| Giovannini et al. 1988 | 0.80 | 0.57 |

Table 5.6: values for the correlation coefficient $r$ and the angular coefficient $m$ for the samples SDSS-FIRST-NVSS-GLEAM and Giovannini et al. 1988 for the plot core power vs. total power.

We have the deviation between the two populations because even if better than the NVSS, the FIRST angular resolution is still much poorer than what

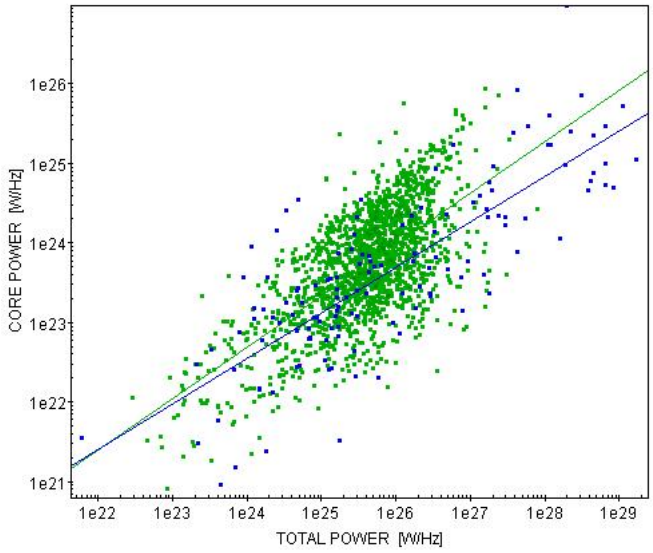


Figure 5.6: core power vs. total power for the sample SDSS-FIRST-NVSS (green) and the sample of Giovannini et al. 1988 (blue). We considered the deamplification of the core emission due to redshift.

Giovannini et al. used to study the correlation; in particular, the jet base can contribute significant flux density when the sources are more distant, since the linear scale corresponding to the FIRST beam becomes larger and thus more affected by extended regions.

Based on the results of radio galaxy population simulations described in Appendix, we determined an empirical correction to rescale the FIRST flux density to provide a more accurate estimate of the core flux density. This is shown in equation (5.2).

$$S\text{core} = \frac{S\text{first}}{(1 + z \times 10)} \quad (5.2)$$

Therefore we estimated a new value for the core power for the population SDSS-FIRST-NVSS-GLEAM, and we plotted the data again.

We deleted the deviation between the samples. Infact we can see a lower difference for the angular coefficients: $\Delta m = 0.64 - 0.57 = 0.07$. However, there are still two problems to solve: the objects of the population SDSS-NVSS-FIRST-GLEAM are not homogeneously distributed, infact the sources density is lower at lower total and core power; also there are no objects with larger total power and lower core power but there are objects with larger total power and larger core power.
Moreover, we applied the correction for the deamplification of the flux density even for the sample AT20G-GLEAM, but we still observed a gap between the AT20G-GLEAM and the population of Giovannini. The gap is only reduced but it still exist with a difference of the angular coefficients $\Delta m = 0.70 - 0.57 = 0.13$. So we have a confirmation of our idea: the AT20G reports only the brightest sources. In other words, the discrepancy in this plot is due to the AT20G sample being biased towards more core-dominated sources, and not an angular resolution effect as in the FIRST case.

| sample | $r$ | $m$ |
|---|---|---|
| SDSS-NVSS-FIRST-GLEAM | 0.66 | 0.64 |
| Giovannini et al. 1988 | 0.80 | 0.57 |

Table 5.7: values for the correlation coefficient $r$ and the angular coefficient $m$ for the samples SDSS-FIRST-NVSS-GLEAM and Giovannini et al. 1988 for the plot core power vs. total power. We considered the deamplification of the core emission due to redshift.

## 5.3 Lobes component and core component in a spectrum of radio loud AGN

We can divide a spectrum of AGN in two components: the extended emission component and the core emission component. The former has a

steep spectrum and it is originated by the lobes, the latter has a flat spectrum and it is originated by the core. The spectrum for an AGN can be approximated by the sum of these two contributions. We want to estimate the ratio between the lobes component and the core component. We have the sample GLEAM, a catalog with a band where both the core component and the lobes component are important. We need consider a spectral index for every component and for the total spectrum. For the lobes component we consider the mean spectral index of the sample GLEAM, where the most sources are lobe dominated in the frequency range 72-231 MHz (infact we detected 747 gamma-ray blazars in the GLEAM sky, where there are 307455 sources). For the core component we consider the mean spectral index of the sample 3LAC-AT20G, this is a sample composed by blazars detected at high frequency (1-20 GHz). For the total spectrum we use the mean spectral index of the sample 3LAC-GLEAM (blazars detected at low frequency).

We can describe the flux density for a source with the relation (5.3):

$$S_{tot} = K_{tot}\nu^{\alpha_{tot}} \quad (5.3)$$

With this formula we show a relation between the flux density and the frequency, using the coefficient $K_{tot}$. We can split the relation (5.3) into two components: the core emission and the extended emission:

$$S_{tot} = K_{core}\nu^{\alpha_{core}} + K_{lobe}\nu^{\alpha_{lobe}} \quad (5.4)$$

So the following relations are right for the lobes and the core:

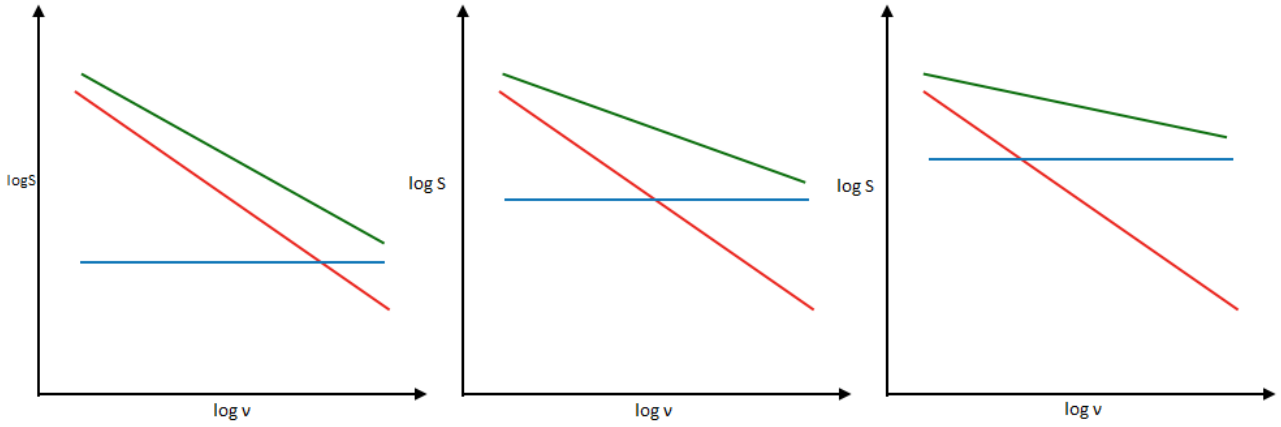


Figure 5.7: three examples for a spectrum of an AGN: the sum of the steep component (red) and the flat component (blue), produces the total spectrum (green). From the first spectrum (left) to the third spectrum (right) ratio between lobe and core emission decreases, and the overall spectrum flattens. In our case, the green line is the GLEAM spectrum, composed of two contributions, and we use it to constrain the relative weight of the extended (red) and nuclear (blue) components.

$$S_{core} = K_{core}\nu^{\alpha_{core}} \quad (5.5)$$

$$S_{lobe} = K_{lobe}\nu^{\alpha_{lobe}} \quad (5.6)$$

Let us consider the definition for the spectral index:

$$\alpha = \frac{\log \frac{S_1}{S_2}}{\log \frac{\nu_1}{\nu_2}} \quad (5.7)$$

where in our case we consider $\nu_1 = 72$ MHz and $\nu_2 = 231$ MHz, while $S_1$ and $S_2$ are the flux density for the two values of frequency. So we used the frequency range of GLEAM and $\alpha$ is the mean spectral index for the total spectrum.

Substituting (5.5) and (5.6) in (5.7), we obtained a relation to explicit the ratio between the lobes coefficient and the core coefficient:

$$\frac{K_{lobe}}{K_{core}} = \frac{-10^{\alpha \log \frac{\nu_1}{\nu_2}} \times \nu_2^{\alpha_{core}} + \nu_1^{\alpha_{core}}}{10^{\alpha \log \frac{\nu_1}{\nu_2}} \times \nu_2^{\alpha_{lobe}} - \nu_1^{\alpha_{lobe}}} \quad (5.8)$$

where $\alpha = 0.45$ and it is the mean spectral index of the sample 3LAC-GLEAM (total spectrum). $\alpha_{core} = -0.05$ and it is the mean spectral index of the sample 3LAC-AT20G (core component). $\alpha_{lobe} = -0.77$ and it is the mean spectral index of GLEAM (lobes component). We obtained a $K_{lobe}/K_{core} \sim 41$. In a previous work, Giroletti et al. 2016, the same ratio is estimated, using MWACS instead of GLEAM. In that work the ratio estimated is $K_{lobe}/K_{core} \sim 75$. The ratio provide a measure for the contribution of the core in the spectrum. We can understand the importance of the core in a spectrum of a source in the Fig. 5.7, where we can see from left to right the core is more important and the flat component contributes at lower frequency. So our work shows that the core is more important than for the work Giroletti et al. 2016. In particular, the survey in Giroletti et al. 2016, has a limited depth, so only the objects with a large extended emission can be observed, therefore the sample overstimates the contribution of these objects. With GLEAM we have a better sensitivity, a larger and deeper survey than MWACS. Therefore, it is evident that the core contribution is underestimated in Giroletti et al. 2016 and now we provide a better measure for the ratio between the core contribution and the lobes contribution.
Also, assuming $K_{lobe}/K_{core} \sim 41$ and varying the frequency, we estimated the ratio between the flux density for the lobes and the flux density for the core. Increasing the frequency the lobes component is fainter, and at 176 MHz we obtain $S_{lobe}/S_{core} \sim 1$. So at 176 MHz the two components have the same importance.

$$\frac{S_{lobes}}{S_{core}} = \frac{K_{lobe}\nu^{\alpha_{lobe}}}{K_{core}\nu^{\alpha_{core}}} \tag{5.9}$$

For $\nu = 176$ MHz:

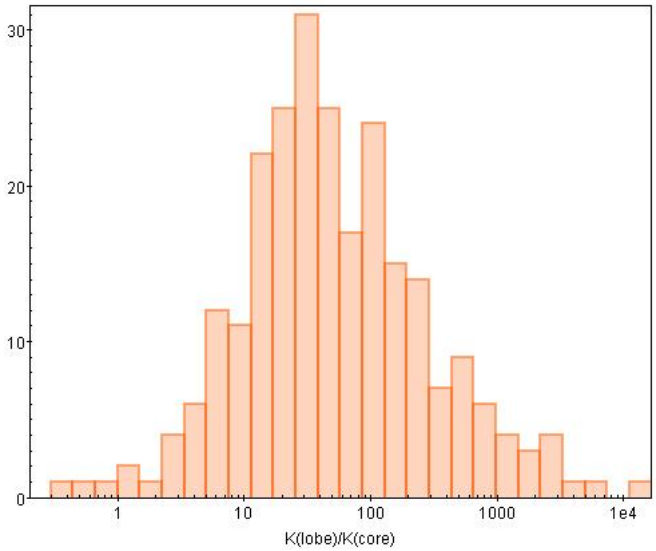


Figure 5.8: distribution of the ratio $K_{lobe}/K_{core}$.

$$\frac{S_{lobes}}{S_{core}} = \frac{K_{lobe}176^{\alpha_{lobe}}}{K_{core}176^{\alpha_{core}}} \sim 1 \tag{5.10}$$

The spectral indices have the same values of the relation (5.8).
Moreover we estimated the ratio $K_{lobe}/K_{core}$ for every object of the sample originated by the cross-correlation 3LAC-GLEAM vs. 3LAC-AT20G. We did not use the mean values for the spectral index but we used the values of the single object. We show an histogram of the logarithm of the ratio in the Fig. 5.8. We can describe the distribution with a Gaussian form (the mean value is about 99), and the graphic show the most sources are lobe dominated. Infact, only for few objects the ratio is close to 1.

# Conclusions

The GLEAM is the deepest and bigger survey at low frequency and our work has improved our knowledge about the spectral properties of blazars and the lobes and radio cores of radio loud AGN.

## Properties of blazars detected at low frequency

For the Unified Model of AGN, the blazars are the aligned counterpart of radio galaxies, infact the BL Lacs are the counterparts of the radio galaxy FRI and the FSRQs are the counterparts of the radio galaxy FRII. The Doppler boosting makes a flat-radio spectrum for the blazars, increasing the radio flux density. So it is very hard to study the extended emission. For this reason the low frequency observations are opening a new window to observe blazars. However, the amplification of the core is apparent. Our study show that the LSP present a flatter spectrum than the HSP. The value of the spectral index for the HSP is $< \alpha >= 0.57$ while for the LSP is $< \alpha >= 0.34$. Before now we considered the blazars like object with the same value for the spectral index, instead now we see different value for two class of the blazars. Since the two populations have also different redshift distributions, it is also possible that this difference is due to the fact that we are probing different parts of the rest-frame spectrum.

Moreover, we seen an interesting correlation between the gamma emission and the radio emission (Fig. 4.6, 4.7, 5.1). The former is produced close to

the base of the jets. Increasing the radio frequency, the correlation is stronger due to the Doppler boosting. This effect regards the radio core.

Also we showed that in the radio band and in the gamma band the LSP and FSRQs are the brightest sources. Instead for the X-rays the brightest sources are the HSP and BL Lacs. The ISP and BCU have intermediate properties. In general the LSP and FSRQs have similar spectral properties, infact the most FSRQs are LSP. In particular, for our data the FSRQs, identified as LSP, are a fraction composed by about 89% of the sample. Also many BL Lacs and the HSP have similar spectral features, infact we seen that about 40% of the BL Lacs are HSP.

## Radio cores and lobes

We studied the behaviour of the core dominance (ratio between the core power and the total power) and we found a correlation (Fig. 5.6). However, the objects are not homogeneously distributed, infact the sources density is lower at lower total and core power; also there are not sources with larger total power and lower core power but there are sources with larger total power and larger core power. So we still have some issues to understand. Also we seen a slightly correlation spectral index $< \alpha >$ vs. ratio flux density $< S_F/S_N >$, where we assumed $S_F$ as core emission and $S_N$ as extended emission. The lobe dominated sources have a lower spectral index (steep spectrum) while the core dominated sources have a larger spectral index (flat spectrum).
Moreover, we studied the ratio between the flat component and the steep component for radio sources and we estimated the ratio $K_{lobe}/K_{core} = 40.63$. This value is lower than the value for the ratio estimated in Giroletti et al. 2016, so we understood that the core contribution is more important in the spectrum, thanks the better technical features of GLEAM respect to

MWACS. Also we seen the distribution of the ratio $K_{lobe}/K_{core}$ for a sample of blazars detected at low and high frequency, and the most sources have a ratio larger than 1 (Fig. 5.8).

At this point, the main part of our work is done. The next part consist in a simulation to compare with data results, and to understand if our method of research is correct. The simulation is in the following Appendix.

# Appendix A

# Code simulation of radio sources

We want to know the core power for a large sample of objects but we have not interferometric images, so we need another method to estimate it. The survey FIRST is ideal for our objective, infact that is a large survey (a covered area of 10000 sq. deg.), a good sensitivity (1 mJy), so we have not bias effects like in the AT20G, where the brightest and core dominated souces are favored. Also we have a good angular resolution (5 arcsec), so this is ideal to study the core. However, we want to understand how much this angular resolution is suitable to describe the core emission. Therefore, we created a simulation of 20000 sources to reproduce the data of the catalogue SDSS-FIRST-NVSS. The radio sources are described by different parameters: redshift, intrinsic size, monochromatic luminosity, angle of viewing and spectral index. Using these parameters, we calculated other properties: luminosity distance, angular diameter distance, projected angular size, Doppler factor, total flux density and peak brightness. We setted a threshold for the peak brightness of 1 mJy (sensitivity of the FIRST). Infact, only 8329 objects are detected in the simulation, while the rest of objects are not detected. In other words, we selected a fraction of objects. So it is possible to estimate the contribution of the extended component (jets and lobes) for these sources.

In particular this component contaminates the core contribution. So it is possible to estimate the contamination of the extended component respect to core component, varying the redshift. Then we could apply a correction to estimate the core power of the real objects (studied in chapter 5).

The simulation has been realized using the code *Python*. In particular we used the package *Anaconda*, where there are *astropy* and *numpy*: two other packages specifically designed to numerical and astrophysical applications. They has been fundamental to realize this work. Infact, using these package we generated some properties (for instance the luminosity distance and the angular diameter distance). Infact these packages contain all useful information for the cosmology of the Universe (density parameter, Hubble constant, etc.). Also *Anaconda* contains *math*, and with this package is possible to execute all useful calculations to generate all parameters.

In the following sections we show the physical parameters of the simulation.

## The redshift distribution

We generated objects distributed in a redshift range between $\sim$0.0 and $\sim$0.7. These numbers are respectively the minimum value and the maximum value for the redshift in the catalogue SDSS-FIRST-NVSS. We generated the distribution, using the following relation:

$$z = (np.random.power(3, nobj)) \times (0.680 - 0.001) + 0.001 \quad \text{(A.1)}$$

where $np.random.power(3, nobj)$ is a function of the code *Python*. It selects a number $nobj$ (in this simulation $nobj = 20000$) of values to create power law distribution of index 2 in the range $0.001 < z < 0.68$.

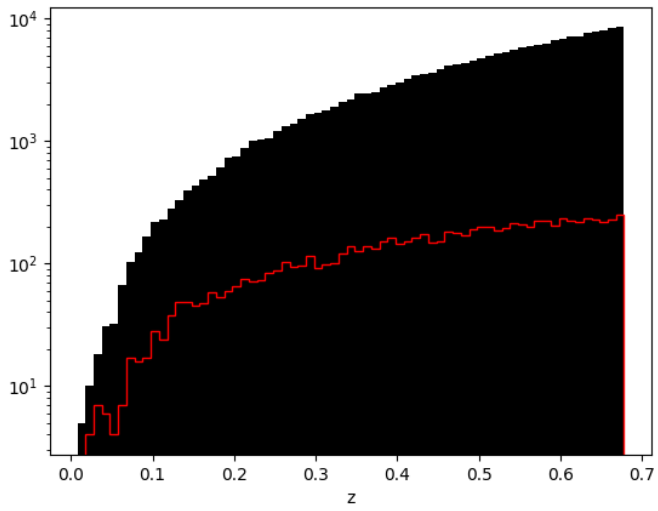


Figure A.1: redshift distribution: the number of sources increases with the redshift. The red curve describes the distribution for the objects detected.

In the redshift distribution (Fig. A.1), increasing the redshift the number of sources increases. Infact, we expect this behaviour for a survey. The red curve describes the histogram for the sources detected, while the objects above this curve, are the sources undetected. In particular, the gap between the detected and undetected sources increases with the redshift. Infact it is more difficult to observe a source at larger redshift.

In each plot, the red curve shows the distribution for the simulated sources that would be detected in the FIRST, while the solid histogram shows the entire population of simulated sources.

## The intrinsic size distribution

The sources are generated with an intrinsic size between 1 Kpc and 1.5 Mpc, according to the typical values for a survey. We generated the distributions, using the following relations:

$$a = np.random.rand(nobj)$$
$$b = a \times (1500000 - 1) + 1$$
$$size = b \times 10^{-6}$$

(A.2)

In the first relation we selected *nobj* random values, in the second relation we generated the values in the range between 1 pc and 1.5 Mpc, and in the third relation we converted the values in units of Mpc.
In this case the distribution is uniform because the probability for every source to have a value of size instead of another value is the same, we assume that the sources grow with constant velocity. But the distribution is not homogeneous for the objects detected by FIRST-NVSS. Infact we observe a larger number of sources with lower intrinsic size. This effect is due to the sensitivity of the FIRST-NVSS. We remember that with a larger intrinsic size, the flux density is distributed in a bigger region and it is easier that the flux density is lower than 1 mJy in every beam. So the sources detected with a large size must have a large enough flux density.

## The viewing angle distribution

We generated the viewing angle distribution with the three following relations:

$$u = np.random.rand(nobj)$$

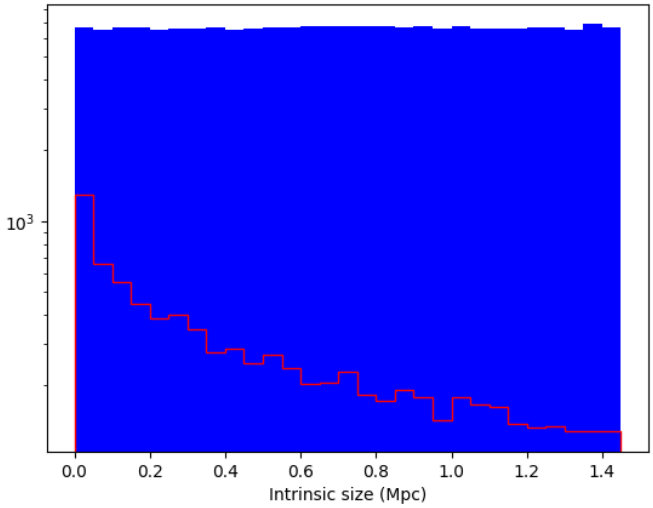


Figure A.2: distribution of intrinsic size of the sources. The red curve describes the distribution for the objects detected.

$$h = arccos(u)$$
$$\theta = \frac{h}{\pi} \times 180 \tag{A.3}$$

With the first equation we created *nobj* uniformly distributed, with the second equation we estimated the reverse function of the cosine of $u$, and using this method (called "inverse function method") we created a 3d angular distribution. In the third equation we converted the values from radiants to degree.

Every radio source presents a viewing angle. This angle is between the approaching jet and the line of sight. According to the Unified Model for AGN, varying the angle we observe a different kind of object. In general in a survey we have more sources with a larger viewing angle than sources

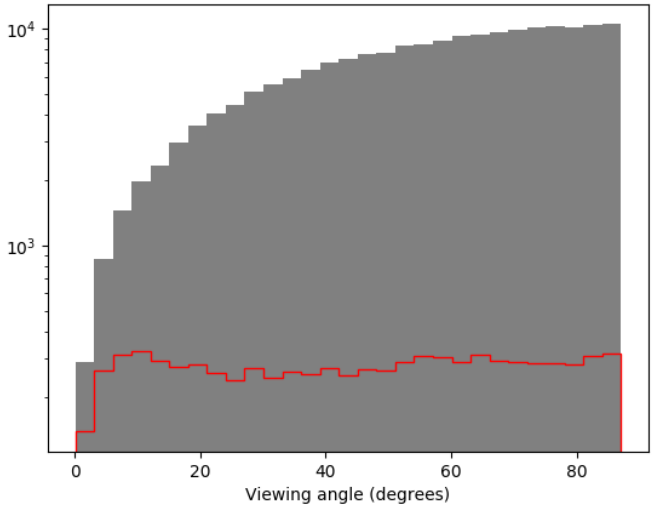


Figure A.3: viewing angle distribution: increasing the angle the number of sources undetected increases. Instead the sources detected do not increase then about 5 degree. The red curve describes the distribution for the objects detected.

with a lower angle. So the blazars are only a little fraction of the radio sources and the most objects are radio galaxies. Infact the viewing angle distribution shows the number of sources increases with the viewing angle. This behaviour what is expected for sources oriented randomly in the space. When we consider only the detected sources, the viewing angle distribution is more homogenehous. We have not a growing behaviour because increasing the angle, the size of every source increases, so it is more difficult to observe an object. We seen this effect in the intrinsic size distribution (Fig. A.4). However, we see that the sources detected increase for very little angles and then the distribution is homogeneous. The distribution increases from 0 to about 5 degree.

## The spectral index distribution

For the spectral index we assumed a Gaussian curve centered at the value -0.7. The relation to create the distribution for *nobj* is the following:

$$\alpha = np.random.normal(-0.7, 0.15, nobj) \tag{A.4}$$

where $-0.7$ is the central value and 0.15 is the associated standard deviation. All objects are described by a Gaussian behaviour. This distribution shows that the most source have a steep spectrum and are lobe dominated. This idea is in agreement with the viewing angle distribution. Infact in that distribution the most sources have a large angle and these objects are lobe dominated, in agreement the Unified Model of AGN.

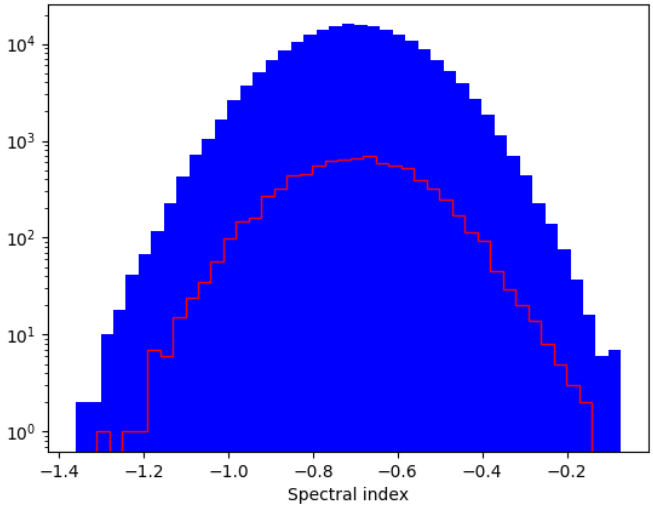


Figure A.4: spectral index distribution: we assumed a Gaussian distribution for all objects. The red curve describes the distribution for the objects detected.

In the previous sections we described the physical parameters generated in the simulations. In the next sections we describe the parameters calculated using the parameters generated. Moreover, in the next pages we report the luminosity distribution. The luminosity is a parameter generated (and not calcuated), but we applyed a correction, using the Doppler factor.

## The luminosity distance and the angular diameter distance distributions

We generated these two parameters with the relations:

$$\mathrm{D}_L = cosmo.luminositydistance(z).value \quad \text{(A.5)}$$

$$\mathrm{d}_A = cosmo.angulardiameterdistance(z).value \quad \text{(A.6)}$$

they are code commands, and they generated the two parameters, using the package *astropy*. We inserted the redshift generated, and the package provided the luminsity distance and the angular diameter distance.

The luminosity distance is a consequence of the redshift distribution. In the latter distribution we have more sources with a larger redshift, so we have more sources with a larger luminosity distance. This behaviour is true for sources undetected and sources detected.

Also the angular diameter distance distribution is a consequence of the redshift distribution and the sources increase at larger values of the diameter.

## The projected angular size distribution

We calculated the projected angular size distribution with the following relations:

$$\begin{gathered} \mathrm{size}_A = \frac{size}{d_A} \\ n = size_A \times \frac{180}{\pi} \\ f = n \times 3600 \\ \delta = f \times sin(\theta) \end{gathered} \quad \text{(A.7)}$$

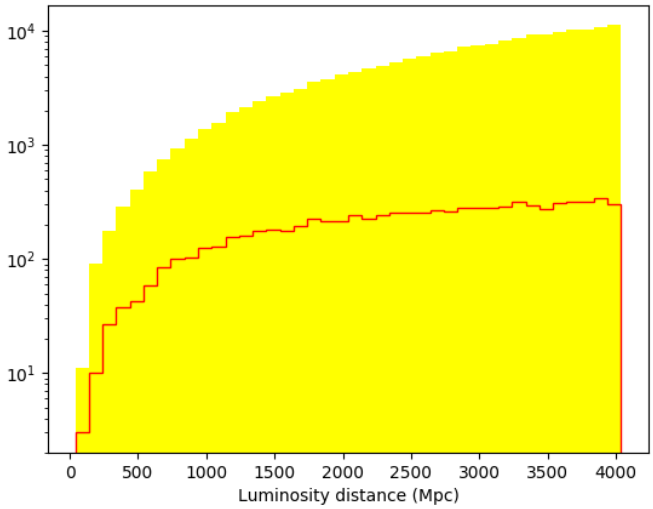


Figure A.5: luminosity distance distribution: increasing the luminosity distance the number of sources increases. The red curve describes the distribution for the objects detected.

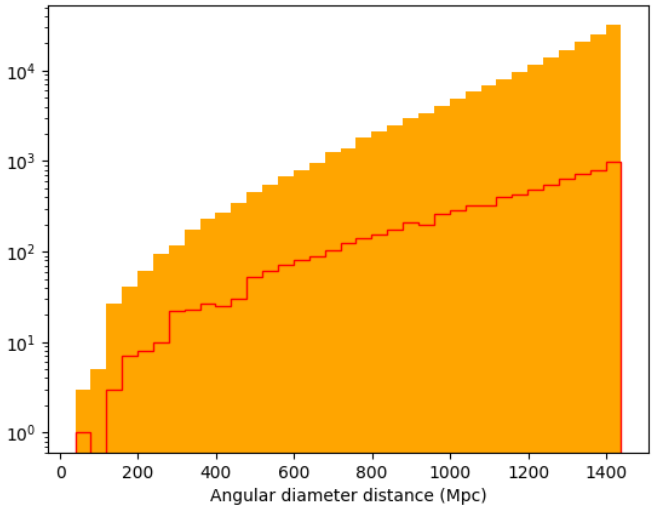


Figure A.6: angular diameter distance distribution: increasing the angular diameter distance the number of sources increases. The red curve describes the distribution for the objects detected.

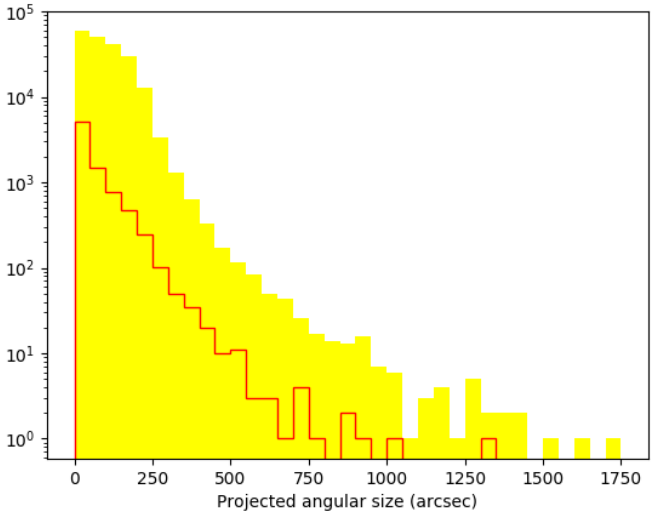


Figure A.7: projected angular size distribution: the number of sources decreases with the size. The red curve describes the distribution for the objects detected.

In the first relation we calculated the angular size with the ratio between the intrinsic size and the angular diameter distance. In the second relation we converted the angular size to degree and in the third relation we converted the same angular size to arcseconds. In the fourth equation we obtained the projected angular size, multiplying the angular size times the sine of the viewing angle.
We show in Fig. A.3 the distribution of the projected angular size: the objects with a larger angular size are those closer to us and we have more sources with a lower angular size. Infact we remember that the number of sources increases with the redshift.

We reported also the distribution for three ranges of angular resolution and we describe these ranges in the Table A.1.

| range of angular resolution [arcsec] | FIRST | NVSS |
|---|---|---|
| <4.5 | point source | point source |
| 4.5-45 | extended source | point source |
| >45 | extended source | extended source |

Table A.1: ranges of angular resolution: we see different visibility of the FIRST and the NVSS.

Also we show the angular size distribution with the ranges in the Fig. A.3. We see the NVSS and FIRST can observe more sources extended than point sources.

## The Doppler factor distribution

The Doppler factor is connected to the viewing angle. So the behaviour of Doppler factor distribution depends on the viewing angle distribution. We show the relation between the Doppler factor and the viewing angle in the formula A.8:

$$\mathrm{D} = \frac{1}{\gamma(1 - \beta\cos\theta)} \quad \text{(A.8)}$$

where $\gamma = \frac{1}{\sqrt{1-\beta^2}}$ is the Lorentz factor, $\beta = \frac{v}{c}$ ($v$ is the velocity of the particles that compose the jets in every radio galaxy, while $c$ is the light velocity) and $\theta$ is the viewing angle. We assumed $\gamma = 5$. Increasing the value of $\theta$, the value of D decreases, and the number of the sources increases. Analyzing the distributions A.7 and A.10 and the relation (A.8) we can see this behaviour. We see a similar behaviour for observed and unobserved objects. The distribution for the observed objects has not the same behaviour of the distribution for the unobserved objects, due to the sensitivity of the

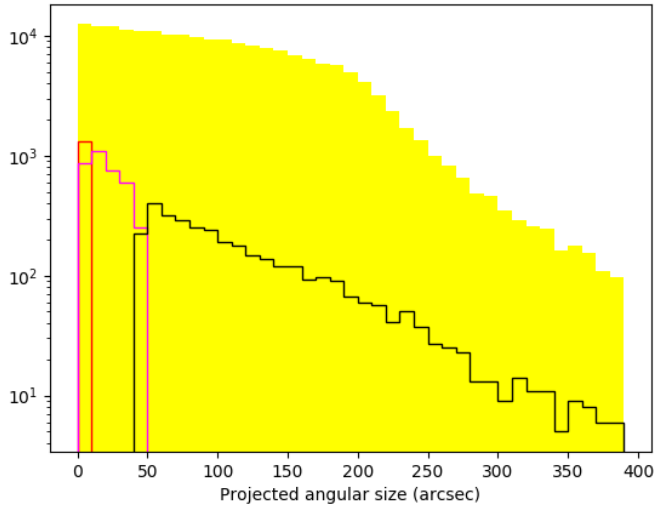


Figure A.8: projected angular size distribution with three ranges: <4.5"(red), 4.5"-45"(magenta), >45"(black).

FIRST-NVSS. To estimate the Doppler factor is necessary to consider the effects of the Doppler boosting. Therefore, the luminosity distribution is connected with the Doppler factor distribution.

## The luminosity distribution

We generated the distribution with the following equation:

$$logL = 27 - 6 \times np.random.power(3, nobj) \quad \text{(A.9)}$$

In this equation 27 is the maximum value of logarithm of the luminosity, instead $27 - 6 = 21$ is the minimum value for the same parameter. The function $np.random.power(3.0, nobj)$ describes a power law distribution of

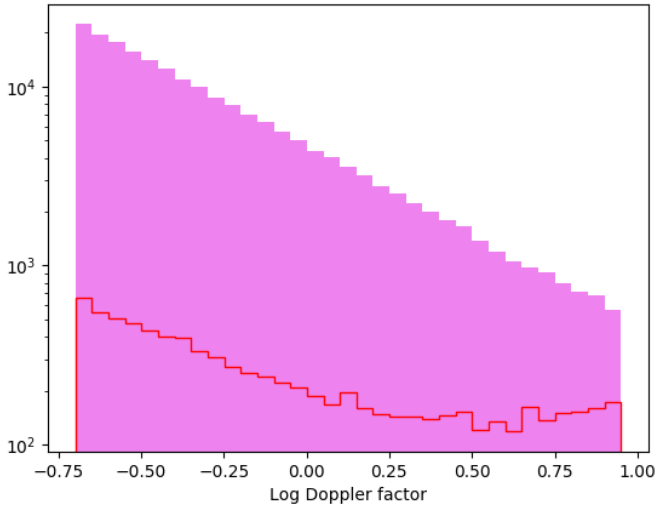


Figure A.9: Doppler factor distribution: we see a similar behaviour for observed and unoberserved objects. The red curve describes the distribution for the objects detected.

index 2.

In a survey the number of sources decreases with the luminosity, and we see this behaviour in the luminosity distribution for the unobserved sources. Instead for the observed sources the number of objects increases and the gap with the sources undetected decreases. Infact at about $10^{26}$ W/Hz the gap is deleted. It is more difficult to detect objects at lower luminosity than at larger luminosity. Also we must consider the effects of the Doppler boosting. This phenomena causes an amplification of the luminosity. To consider this effect we used the relation A.10:

$$\mathrm{L} = 0.1 \times 10^{n} \times D^{3+\alpha} + 0.9 \times 10^{n} \quad \text{(A.10)}$$

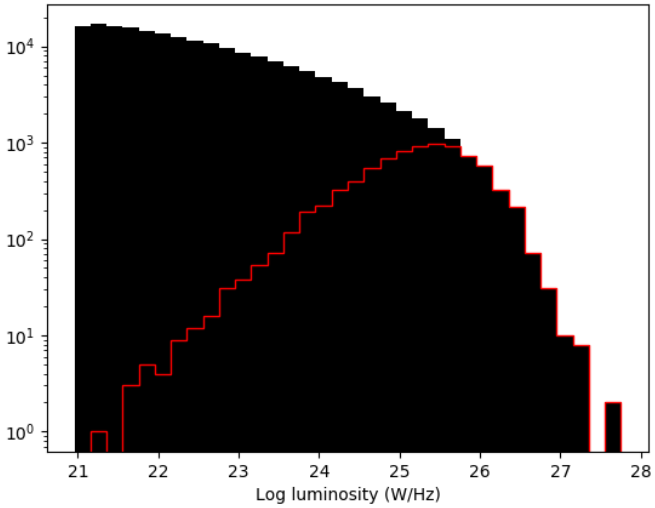


Figure A.10: luminosity distribution: the number of the sources undetected decreases with the luminosity, while for the sources detected is true the opposite. The red curve describes the distribution for the objects detected.

where n is the logarithm of the luminosity (in our simulation we have values in a range between 22 and 27 if we do not consider the Doppler boosting, and we have values in a range between 22 and 28 considering the Doppler boosting), $D$ is the Doppler factor, and $\alpha$ is the spectral index. The formula contains the component for the core and the component for the lobes. In particular, the component of the core is described by $0.1 \times 10^n \times D^{3+\alpha}$, where the exponent $3 + \alpha$ considers the presence of synchrotron radiation and the term 0.1 considers the limited extension of the core in a radio galaxy. The component of the lobes is described by $0.9 \times 10^n$ and 0.9 considers the large extension of the lobes; the lobes do not have a Doppler beaming factor because we assume them not to have a relativistic bulk motion.

## The flux density distribution

We calculated the flux density with the following two equations:

$$\text{s}= \frac{L}{4\pi \times D_L^2}$$
$$S = s \times 10^{29}$$

(A.11)

With the first relation we estimated the flux density for the International System (L and $D_L$ are the luminosity and the luminosity distance). Instead in the second equation we converted the flux density to mJy.

The flux density distribution shows the observed and unobserved sources divided by the threshold of the sensitivity of the FIRST and the NVSS. We remember that the two catalogues have a similar sensitivity, infact they a sensitivity of about 1 mJy. So every source below this limit is undetected. Increasing the flux density, the number of sources decreases. In a survey the most sources are faint and we just observe the brightest sources. To increase the number of sources detected we must have a lower sensitivity.

## Statistical data of the simulation and conclusions

In this section we report the statistics about the physical parameters as yet described for the objects detected. Also we report the parameters for the true catalog SDSS-FIRST-NVSS and the sample originated with the cross-correlation between SDSS-FIRST-NVSS and GLEAM. So we compared the values of the simulation with the values of the true data. The values of the simulation have about the same order of magnitude of the true catalogues. However some parameters of the simulation are not in the true catalogues.

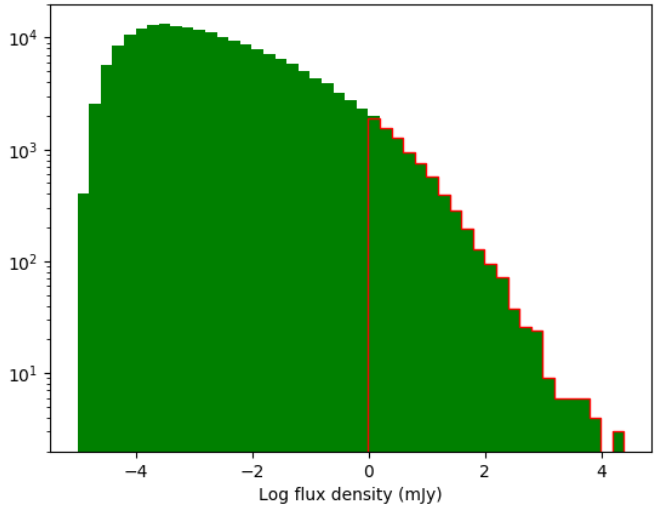


Figure A.11: flux density distribution: we observe only the sources over 1 mJy. The red curve describes the distribution for the objects detected.

They are the intrinsic size, the projected angular size, the viewing angle, the Doppler factor. Also we have the spectral index only in the sample with GLEAM. We have to specify that the logarithm of flux density for the FIRST is estimated only for 15550 objects (the entire sample is composed by 18286 objects) in the SDSS-FIRST-NVSS catalog. While in the catalog generated with the cross-match the logarithm of the flux density of the FIRST is estimated only for 2217 objects (the entire sample is composed by 2906 objects).

| parameter | symbol |
|---|---|
| redshift | z |
| intrinsic size [Mpc] | size |
| luminosity distance [Mpc] | $D_L$ |
| angular diameter distance [Mpc] | $d_A$ |
| angular size [arcsec] | $\delta$ |
| viewing angle [degree] | $\theta$ |
| log Doppler factor | log D |
| spectral index | $\alpha$ |
| log luminosity [W/Hz] | log L |
| log flux density [mJy] | log S |

Table A.2: legend for the physical parameters.

The values of the simulation are similar to the values of the true catalogues so we realized an useful simulation to reproduce a real survey.

Moreover, we divided the sample of the sources detected in seven bins redshift. We estimated the mean value of the angular size for every bin. For the lowest values of the redshift, the beam for the FIRST-NVSS corresponds to about 1/100 of a radio galaxy. Instead, for the largest values of the redshift, the beam corresponds to about 1/14 of a radio galaxy. In other words, increasing the redshift, a bigger region of a radio galaxy is included in the beam of the FIRST-NVSS. So the contribution of the extended region (so of the jets and the lobes) is more important. Therefore, the FIRST is more suitable to estimate the core power at lower redshift. We reported the mean angular size and the number of the beam included in a radio source for every redshift bin in the Table A.4. From these numbers, we have determined a correction factor that we applied to the observed FIRST flux density for each source to estimate the core flux density used for the core dominance study carried out in Chapter 5.

| parameter | mean value1 | SD1 | mean value2 | SD2 | mean value3 | SD3 |
|---|---|---|---|---|---|---|
| redshift | 0.46 | 0.15 | 0.23 | 0.14 | 0.24 | 0.13 |
| size [Mpc] | 0.5 | 0.4 | | | | |
| $D_L[Mpc]$ | 2630 | 980 | 1220 | 810 | 1260 | 770 |
| $d_A[Mpc]$ | 1170 | 260 | 720 | 350 | 750 | 320 |
| $\delta[arcsec]$ | 100 | 100 | | | | |
| $\theta[degree]$ | 46 | 26 | | | | |
| log D | -0.1 | 0.5 | | | | |
| $\alpha$ | -0.70 | 0.15 | | | -0.6 | 0.3 |
| log L [W/Hz] | 25.1 | 0.9 | 23.8 | 0.9 | 24.2 | 0.9 |
| | | | 24.1 | 0.9 | 24.6 | 0.8 |
| log S [mJy] | 1.0 | 0.8 | 0.9 | 0.4 | 1.2 | 0.5 |
| | | | 1.2 | 0.4 | 1.6 | 0.5 |

Table A.3: physical parameters (see the Table A.2) with the associated errors. We indicate with meam value1 and SD1 the mean value and the associated error of the simulation, mean value2 and SD2 are the measures of the true catalog SDSS-FIRST-NVSS. Instead mean value3 and SD3 are the measures of the the cross-correlation SDSS-FIRST-NVSS vs. GLEAM. For the luminosity and the flux density we have two values of the true samples. In the upper line we have the values of the FIRST, while in the bottom line we have the values of the NVSS.

A possible development of this simulation for the future, it could be to execute an estimate of the core dominance and then to compare the real data (showed in Chapter 5) with the simulated data, to verify the correct efficiency of our method of research with the real data. In the future, this simulation could be extended or it could be compared with other similar projects. The latter could be useful to analyze radio sources detected by SKA (Wittham et al. 2016).

| redshift bin | <angular size> [arcsec] | number of beams |
|---|---|---|
| 0-0.1 | 458 | 102 |
| 0.1-0.2 | 211 | 47 |
| 0.2-0.3 | 141 | 31 |
| 0.3-0.4 | 105 | 23 |
| 0.4-0.5 | 86 | 19 |
| 0.5-0.6 | 74 | 16 |
| 0.6-0.7 | 65 | 14 |

Table A.4: mean angular size and number of beams included in a radio galaxy for every redshift bin.

# Bibliography


[1] Abazajian, K., N., Adelman-McCarthy, J. K., Agueros, M. A., et al. 2009, ApJS, 182, 543

[2] Acero, F., Ackermann, M., Ajello, M., et al. 2015, ApJS, 218, 23

[3] Ackermann, M., Ajello, M., Atwood, W. B., et al. 2015, ApJ, 810, 14

[4] Atwood, W. B., Abdo, A. A., Ackermann, M., et al. 2009, ApJ, 697, 1071

[5] Baldi, R. D., Capetti, A., Giovannini, G., et al. 2015, A&A, 576, A38

[6] Becker, R. H., White, R. L., Helfand, D. J., et al. 1995, ApJ, 559, 577

[7] Best, P. N., Heckman, T. M., et al. 2012, MNRAS, 1569, 1582

[8] Condon, J. J., Cotton, W. D., Greisen, E. W., Yin, Q. F., et al. 1998, ApJ, 1693, 1716

[9] Donato, D., Ghisellini, G., Tagliaferri, G., Fossati, G., 2001, A&A, 375, 739

[10] Ghisellini, G., Celotti, A., Fossati, G., Maraschi, L., Comastri, A. 1998, MNRAS, 301, 451

[11] Giovannini, G., Feretti, L., Gregorini, L., Parma, P. et al. 1988, A&A, 73, 84

[12] Giroletti, M., Massaro, F., D'Abrusco, R., et al. 2016, A&A, 588, A141

[13] Hada, K., Kino, M., Doi, A., et al. 2016, ApJ, 817, 131

[14] Hurley-Walker, N., Morgan, J., Wayth, R. B., et al 2014, PASA, 31, e045

[15] Hurley-Walker, N., Callingham, J. R., Hancock, P. J., et al 2017, MNRAS, 1, 30

[16] Jackson, C. A., Franzen, T. M. O., Seymour, N., et al. 2016, arXiv, arXiv: 1604.04041v1

[17] Mahony, E. K., Sadler, E. M., Croom, S. M., et al. 2011, MNRAS, 417, 2651

[18] Massaro, E., Giommi, P., Leto, C., et al. 2009, A&A, 495, 691

[19] Massaro, F., D'Abrusco, R., Giroletti, M., et al. 2013a, ApJS, 207, 4

[20] Massaro, F., D'Abrusco, R., Paggi, A., et al 2013b, ApJS, 206, 13

[21] Massaro, F., Landoni, M., D'Abrusco, R., et al. 2015, A&A, 575, A124

[22] Moshir, M., Kopman, G., Conrow, T. A. O., et al. 1992, IRAS Faint Source Survey, Explanatory supplement version 2, IPAC, California Institute of Technology

[23] Nori, M., Giroletti, M., Massaro, F., et al. 2014, ApJS, 212, 3

[24] Urry, C. M., & Padovani, P. 1995, PASP, 107, 803

[25] Whittam, I. H., Jarvis, M. J., Green, D. A., et al. 2016, MNRAS, 1, 6

# Ringraziamenti

Colgo l'occasione per ringraziare Marcello Giroletti, per la grande pazienza e la guida offerta in questi mesi. Soprattutto lo ringrazio per aver avuto a cuore il mio futuro e di come si sia interessato alle mie ambizioni. Lo ringrazio perchè è stato un maestro e anche un amico.
Ringrazio il prof. Gabriele Giovannini per la disponibilità avuta in questi anni, sin dai tempi della laurea triennale. Professore sempre attento alle esigenze dello studente. Lo ringrazio perchè con lui ho compiuto i primi passi nell'astrofisica: un lavoro, una scienza ma soprattutto una passione!
Nel corso di questi anni ho avuto tanti amici, così tanti che per ringraziarli tutti dovrei scrivere un libro. Li ringrazio tutti e qualcuno riceverà dei ringraziamenti a parte. Il percorso di questi anni è stato un cammino lungo e difficile, che mi ha messo a dura prova più di una volta. In particolar modo nel periodo iniziale. Anche per questo ringrazio chi mi ha aiutato.
Infine ringrazio i miei genitori per gli immensi sacrifici compiuti in questi anni.....e grazie a mia sorella Federica, per aver tanto spinto perchè andassi a Bologna e aver creduto in me.